KeA1

CHINESE ROOTS
GLOBAL IMPACT

Contents lists available at ScienceDirect

# Petroleum Science

journal homepage: www.keaipublishing.com/en/journals/petroleum-science



# Original Paper

# Numerical investigation on 2-D NMR response mechanisms and the frequency conversion of petrophysical parameters in shale oil reservoirs



Ji-Long Liu, Ran-Hong Xie \*, Jiang-Feng Guo, Guo-Wen Jin

State Key Laboratory of Petroleum Resources and Engineering, China University of Petroleum (Beijing), Beijing, 102249, China

#### ARTICLE INFO

Article history:
Received 11 January 2024
Received in revised form
10 February 2025
Accepted 13 March 2025
Available online 14 March 2025

Edited by Meng-Jiao Zhou

Keywords: Shale oil  $T_1$ - $T_2$  spectra Improved random walk algorithm Frequency conversion

#### ABSTRACT

Characterizing the petrophysical properties holds significant importance in shale oil reservoirs. Two-dimensional (2-D) nuclear magnetic resonance (NMR), a nondestructive and noninvasive technique, has numerous applications in petrophysical characterization. However, the complex occurrence states of the fluids and the highly non-uniform distributions of minerals and organic matter pose challenges in the NMR-based petrophysical characterization. A novel  $T_1$ - $T_2$  relaxation theory is introduced for the first time in this study. The transverse and longitudinal relaxivities of pore fluids are determined based on numerical investigation and experimental analysis. Additionally, an improved random walk algorithm is proposed to, on the basis of digital shale core, simulate the effects of the hydrogen index (HI) for the organic matter, echo spacing ( $T_{\rm E}$ ), pyrite content, clay mineral type, and clay content on  $T_1$ - $T_2$  spectra at different NMR frequencies. Furthermore, the frequency conversion cross-plots for various petrophysical parameters influenced by the above factors are established. This study provides new insights into NMR-based petrophysical characterization and the frequency conversion of petrophysical parameters measured by laboratory NMR instruments and NMR logging in shale oil reservoirs. It is of great significance for the efficient exploration and environmentally friendly production of shale oil.

© 2025 The Authors. Publishing services by Elsevier B.V. on behalf of KeAi Communications Co. Ltd. This is an open access article under the CC BY-NC-ND license (http://creativecommons.org/licenses/by-nc-nd/

4.0/).

#### 1. Introduction

In recent years, the demand for energy has greatly increased. The development of renewable energy sources such as solar, geothermal energy, and wind, alongside conventional fossil fuels, cannot meet current energy needs (Esen and Yuksel, 2013; Van Erdeweghe et al., 2018; Sun et al., 2018a,b). The pressures of energy shortages have prompted exploration into shale oil and gas (Zhan et al., 2020; Liu et al., 2022), which has received great attention from scholars (Zamiri et al., 2022). Shale oil and gas can be economically recovered from shale through hydraulic fracturing, superheated steam injection, and pyrolysis exploitation technology (Osiptsov, 2017; Sun et al., 2017; Sun et al., 2018a,b; Xu et al., 2023; Jiang et al., 2023; Nie, 2023). Furthermore, shale can store large amounts of waste, such as CO<sub>2</sub>, due to its low permeability. Thus, in shale oil reservoirs, investigating the petrophysical properties is

et al., 2023b; Hu et al., 2018; Xu et al., 2023).

Two-dimensional nuclear magnetic resonance (2-D NMR), a nonintrusive and nondestructive technique, can be used to perform petrophysical characterization of reservoirs by detecting the signals of pore fluids (Washburn and Birdwell, 2013; Kausik et al., 2011). The petrophysical characterization of fluids can be acquired based on NMR *T*<sub>1</sub>-*T*<sub>2</sub> spectra (Zhang et al., 2020; Jiang et al., 2018, 2019; Silletta et al., 2023; Kausik et al., 2017), employing both experi

crucial (Liu et al., 2024a). However, the complex occurrence states of fluids and the high heterogeneity of minerals, as well as organic

matter (OM), in shale pose challenges in petrophysical characterization (Dou and Wang, 2022; Liu et al., 2024b; Wang et al., 2023a).

This, in turn, presents further challenges to environmentally

friendly shale production and safe waste storage in shale (Wang

Silletta et al., 2022; Kausik et al., 2017), employing both experimental analysis and numerical simulations. Experimental analysis can directly determine the petrophysical properties, adapting to different magnetic field frequencies for precise petrophysical properties characterization (Fleury et al., 2013; Fleury and Romero-Sarmiento, 2016; Ma et al., 2020). However, experimental analysis does not consider the effects of the heterogeneity of minerals and

E-mail address: xieranhong@cup.edu.cn (R.-H. Xie).

<sup>\*</sup> Corresponding author.

OM across different shale samples (Zhu et al., 2021; Li et al., 2020). In addition, the frequency differences between NMR logging and laboratory NMR instruments can result in differences of petrophysical properties, posing difficulties in the petrophysical characterization of actual formations based on  $T_1$ - $T_2$  spectra. Therefore, it is of great significance to characterize the complex heterogeneity of minerals and OM by NMR  $T_1$ - $T_2$  responses.

In shale oil reservoirs, unlike experimental analysis, numerical simulation techniques can directly reflect their effects on the petrophysical properties. Moreover, numerical investigations can quantify the effects of different factors. However, very few scholars have conducted numerical simulation investigations of  $T_1$ - $T_2$  due to the unclear  $T_1$ - $T_2$  relaxation theory in shale oil reservoir. Currently, there are two main theories concerning the NMR  $T_1$ - $T_2$  relaxation of pore fluids. One theory states that the dipole-dipole interactions caused by protons within and between hydrocarbon molecules are dominant (Bloembergen et al., 1948; Yang and Hirasaki, 2008; Kausik et al., 2018; Yang et al., 2012; Singer et al., 2018; Zhang and Daigle, 2017; Singer et al., 2020), while the other theory argues that the heteronuclear dipole-dipole interactions involving protons within hydrocarbon molecules and the paramagnetic sites from OM are dominant (Benamsili et al., 2014; Korb, 2018; Korb et al., 1996, 1997, 1999, 2014, 2015). Recently, Zhang and Daigle (2017) conducted experiments in which they mixed kerogen (without iron and manganese ions) with water, acetone, chloroform, and cyclohexane, then compared the  $T_2$  values of the deuterated compounds of different fluids and their mixtures with kerogen. They confirmed that OM without iron or manganese ions has NMR response characteristics. They also pointed out that the intramolecular dipoledipole interactions controlled the relaxation for oil, and it depends on the adsorption capacity of <sup>1</sup>H at surface layer, which depends on the adsorbate concentration at surface adsorption sites rather than the proton density of the surface layer, and that spin relaxation is controlled by molecular spins and the proton desorption process. They derived an expression for surface relaxivity according to proton dipole-dipole relaxation theory (the ZD model) (Zhang and Daigle, 2017). Tandon and Heidari (2019) developed an NMR relaxation theory for organic shale. Based on this theory, they determined the longitudinal surface relaxivity ( $\rho_1$ ) and transverse surface relaxivity  $(\rho_2)$  of pore fluids and accurately quantified the transverse relaxation time  $(T_2)$  and longitudinal relaxation time  $(T_1)$  of protons in organic pores (Tandon and Heidari (2019)). The theories proposed by Zhang and Daigle (2017) and Tandon and Heidari (2019) are based on proton dipole-dipole interactions, but these theories have not been adequately verified by experiments on real pore fluids. Korb (2018) confirmed the reasonability of the theory supporting the dominance of heteronuclear dipole-dipole interactions by testing the frequency dependence from oil and experimentally verifying that the dipole-dipole interactions involving protons in pore fluids and VO<sup>2+</sup> in bitumen control the NMR relaxation characteristics of organic pore fluids in shale oil reservoirs; consequently, the protons in organic pore fluids exhibit one-dimensional motion. The heteronuclear dipole-dipole interactions between protons in petrophysical properties and paramagnetic ions such as manganese and iron ions on mineral surfaces control the NMR relaxation for inorganic pore (IP) fluids in shale, due to which the protons in IP exhibit two-dimensional motion. While Korb (2018) improved the theories of the  $T_1$ - $T_2$  relaxation for pore fluids in shale oil, they ignored the characteristics and effects of the NMR relaxation of OM. The plateau (P) model proposed by Singer et al. can be used to describe the strong frequency dependence of the  $T_1$  of OM and the weak frequency dependence of the  $T_2$  of OM (Singer et al., 2020).

Currently, numerical investigations of  $T_1$ - $T_2$  conducted on shale oil reservoirs have mainly focused on the theoretical simulation of

simple equations. Another study explained the NMR relaxation of pore fluids in shale according to the homonuclear dipole-dipole relaxation theory. They simulated changes in relaxation dependence at different angles using rhombic pores with different aspect ratios, and established the Washburn-Mu-Tolke theory grounded in homonuclear dipole-dipole relaxation theory for both organic and inorganic pores (Washburn, 2014; Washburn et al., 2015), However, their theoretical modeling solely selected and used pore radius as a simulation parameter, leading to differences between the results of theoretical modeling and simulations of real shale samples. Chi et al. (2015) accounted for changes in wettability's impact on numerical simulation results, whereas Tandon et al. (2017) developed a finite volume-based inversion recovery-Carr-Purcell-Meiboom-Gill (IR-CPMG) simulation technique, employing pore-scale images of rock samples, topological structures of different fluids (phases), and bulk and surface properties of fluids. They verified the effectiveness of the simulation technique using digital sandstone and carbonate cores containing spherical pores (Tandon et al. (2017)). Building upon the aforementioned work, Tandon and Heidari (2019) simulated the  $T_1$ - $T_2$  responses of hydrocarbons in ellipsoidal pores of organic-rich mudstone samples and the organic pores provided based on focused ion beam scanning electron microscope (FIB-SEM) images (Tandon and Heidari (2019)). However, in their study, the proton dipole-dipole relaxation theory was solely considered from NMR relaxation for oil rather than the OM and water. Meanwhile, the influences on  $T_1$ - $T_2$  responses from the internal magnetic field gradient were not considered.

There are several deficiencies in the published articles on NMR  $T_1$ - $T_2$  numerical simulations of shale oil reservoirs. (a)  $T_1$ - $T_2$  relaxation theories are unclear, and few theories, describing the frequency dependence from pore fluids, OM, and the internal magnetic field gradient, are used for petrophysical properties characterization. (b) The effects from the complex occurrence states of pore fluids and the heterogeneity of minerals and OM on the 2-D NMR  $T_1$ - $T_2$  response are not considered. (c) The effects from the complex occurrence states of pore fluids, the heterogeneous distributions of minerals and OM on petrophysical properties are not considered.

Herein, a  $T_1$ - $T_2$  relaxation theory is proposed to characterize the frequency dependences for OM longitudinal and transverse bulk relaxation times ( $T_{1B,K}$ ,  $T_{2B,K}$ ), the longitudinal and transverse relaxivities for pore fluids ( $\rho_{1S,O}$ ;  $\rho_{1S,W}$ ;  $\rho_{2S,O}$ ;  $\rho_{2S,W}$ ), and internal magnetic field gradient. This theory was verified by the numerical simulations and experiments in this article. The  $\rho_{1\text{S},\text{O}}$ ,  $\rho_{1\text{S},\text{W}}$ ,  $\rho_{2\text{S},\text{O}}$ , and  $\rho_{2SW}$  were determined based on the numerical simulations and experimental analysis, including extraction experiments, multi-frequency  $T_2$  experiments, and 2-D  $T_1$ - $T_2$  experiments conducted on parallel samples of digital shale cores. In addition, the improved random walk (IRW) algorithm was used for the first time to simulate the influences of parameters such as the hydrogen index (HI) of the organic matter, echo spacing ( $T_{\rm E}$ ), pyrite content. clay mineral type, and clay content on the  $T_1$ - $T_2$  responses in shale oil reservoirs at different frequencies based on digital core technology. Frequency conversion cross-plots for various petrophysical properties derived from  $T_1$ - $T_2$  spectra affected by the above factors were established.

#### 2. Theory

#### 2.1. $T_1$ - $T_2$ relaxation theory

For the first time, we have developed an improved Korb's theory for two-dimensional NMR  $T_1$ - $T_2$ , premised on the assumption that water only exists in the IP and oil only exists in the OP. According to Korb's model of  $T_1$ - $T_2$  relaxation theory, the longitudinal and

transverse bulk relaxation rates for pore fluids were determined due to intermolecular and intramolecular dipole-dipole interactions. Additionally, the longitudinal and transverse surface relaxation rates of pore fluids were determined, and the diffusion relaxation rates were determined based on the magnetic-dipole theory. The longitudinal and transverse relaxation rates of organic matter  $(1/T_{1K}, 1/T_{2K})$  are determined by longitudinal and transverse bulk relaxation rates  $(1/T_{1B,K}; 1/T_{2B,K})$ . They can be expressed as

$$\begin{cases} \frac{1}{T_{1L}} = \frac{1}{T_{1RB,L}} + \frac{1}{T_{1TB,L}} + \frac{1}{T_{1S,L}} \\ \frac{1}{T_{1K}} = \frac{1}{T_{1B,K}} \\ \frac{1}{T_{2L}} = \frac{1}{T_{2RB,L}} + \frac{1}{T_{2TB,L}} + \frac{1}{T_{2S,L}} + \frac{1}{T_{2D,L}} \\ \frac{1}{T_{2K}} = \frac{1}{T_{2B,K}}, \end{cases}$$
(1)

where the subscript L represents water (W) or oil (O), while  $T_{\rm 2TB,L}$  and  $T_{\rm 2RB,L}$  denote the bulk relaxation times for pore fluids driven by intermolecular and intramolecular dipole-dipole interactions, and they may be described by the L-S and the B-P-P theories, respectively (Tandon and Heidari, 2019; Lipari and Szabo, 1982).  $T_{\rm 2TB,L}$  and  $T_{\rm 2RB,L}$  could be determined from numerical simulations in combination with extraction and gas chromatography (GC) experiments (Liu et al., 2024c).  $T_{\rm 1TB,L}$  and  $T_{\rm 1RB,L}$  could be determined by the same method.  $T_{\rm 1B,K}$  and  $T_{\rm 2B,K}$  are the longitudinal and transverse bulk relaxation times of organic matter (kerogen and bitumen)

molecules, the  $T_{\rm 1B,K}$  and  $T_{\rm 2B,K}$  exhibited frequency dependence, which can be described by the P model (Singer et al., 2020) and expressed as

$$\begin{cases} \frac{1}{T_{1B,K}} \approx \frac{3}{20} \left(\frac{\mu_{0}}{4\pi}\right)^{2} \gamma^{4} h^{2} \frac{1}{N} \sum_{i=1}^{N} \sum_{j!=i}^{N} \frac{k}{r_{ij}6} \left[ J_{P}(0, \tau_{R,L}, \tau_{l,L}) + 4J_{P}(2\omega, \tau_{R,L}, \tau_{l,L}) \right] \\ \frac{1}{T_{2B,K}} \approx \frac{3}{20} \left(\frac{\mu_{0}}{4\pi}\right)^{2} \gamma^{4} h^{2} \frac{1}{N} \sum_{i=1}^{N} \sum_{j!=i}^{N} \frac{k}{r_{ij}6} \left[ \frac{3}{2} J_{P}(0, \tau_{L}, \tau_{l,L}) + \frac{5}{2} J_{P}(\omega, \tau_{L}, \tau_{l,L}) \right] \\ +J_{P}(2\omega, \tau_{L}, \tau_{l,L}) \right] \\ \tau_{K} = \frac{4\pi}{3K_{B}} R_{R,K}^{3} \frac{\eta_{K}}{T} \\ J_{P}(\omega, \tau_{K}, \tau_{l,K}) = \left( \left( 1 - s_{K}^{2} \right) \frac{2\tau_{K}}{1 + \omega \tau_{K}} + s_{K}^{2} \frac{2\tau_{l,K}}{1 + \omega \tau_{l,K}} \right) \end{cases}$$

$$(2)$$

In addition,  $1/T_{\rm 2D,L}$  in the modified Korb's model denotes the diffusion relaxation rate for pore fluids, which is related to the diffusion coefficient ( $D_{\rm L}$ ), gyromagnetic ratio ( $\gamma$ ), internal magnetic field gradient ( $G_{\rm Z}$ ), and  $T_{\rm E}$ , can be expressed as

$$\frac{1}{T_{2D,L}} = \frac{D_{L}(\gamma G_{z} T_{E})^{2}}{12}$$
 (3)

The  $G_z$  exhibited frequency dependence, can be determined on the basis of the magnetic dipole theory (Liu et al., 2024c). In Eq. (1),  $1/T_{1S,L}$  and  $1/T_{2S,L}$  denote the longitudinal and transverse relaxation rates of water or oil, the  $1/T_{1S,L}$ ,  $1/T_{2S,L}$ ,  $1/T_{1S,O}$ , and  $1/T_{2S,O}$  may be determined on the basis of the modified Korb's model and expressed as

$$\begin{cases} \frac{1}{T_{1S,W}} = \left(\frac{\mu_0}{4\pi}\right)^2 \pi \backslash \left/ \left(30 d \delta_W^2\right) \cdot \sigma_{S,W} \rho_W S_{p,NMR,W} (\gamma_1 \gamma_5 h)^2 S(S+1) \tau_{m,W} \cdot \\ \left[ 3 \ln \left( \frac{1 + \omega_1^2 \tau_{m,W}^2}{\left(\frac{\tau_{m,W}}{\tau_{s,W}}\right)^2 + \omega_1^2 \tau_{m,W}^2} \right) + 7 \ln \left( \frac{1 + \omega_5^2 \tau_{m,W}^2}{\left(\frac{\tau_{m,W}}{\tau_{s,W}}\right)^2 + \omega_5^2 \tau_{m,W}^2} \right) \right] \\ \frac{1}{T_{2S,W}} = \left( \frac{\mu_0}{4\pi} \right)^2 2 \pi / \left( 30 d \delta_W^2 \right) \cdot \sigma_{S,W} \rho_W S_{p,NMR,W} (\gamma_1 \gamma_5 h)^2 S(S+1) \tau_{m,W} \cdot \\ \left[ 2 \ln \left( \frac{\tau_{s,W}}{\tau_{m,W}} \right) + \frac{3}{4} \ln \left( \frac{1 + \omega_1^2 \tau_{m,W}^2}{\left(\frac{\tau_{m,W}}{\tau_{s,W}}\right)^2 + \omega_1^2 \tau_{m,W}^2} \right) + \frac{13}{4} \ln \left( \frac{1 + \omega_5^2 \tau_{m,W}^2}{\left(\frac{\tau_{m,W}}{\tau_{s,W}}\right)^2 + \omega_5^2 \tau_{m,W}^2} \right) \right] \\ \frac{1}{T_{1S,O}} = \left( \frac{\mu_0}{4\pi} \right)^2 \sqrt{2} / \left( 15 \pi R \delta_O^2 \right) \cdot \sigma_{S,O} \rho_0 S_{p,NMR,O} (\gamma_1 \gamma_5 h)^2 S(S+1) \sqrt{\tau_{m,O} \cdot \tau_{S,O}} \cdot \\ \left[ \frac{3 \sqrt{1 + \sqrt{1 + \omega_1^2 \tau_{s,O}^2}}}{\sqrt{1 + \omega_1^2 \tau_{s,O}^2}} + \frac{7 \sqrt{1 + \sqrt{1 + \omega_5^2 \tau_{s,O}^2}}}{\sqrt{1 + \omega_5^2 \tau_{s,O}^2}} \right] \\ \frac{1}{T_{2S,O}} = \left( \frac{\mu_0}{4\pi} \right)^2 \cdot 2 / \left( 15 \pi R \delta_O^2 \right) \cdot \sigma_{s,O} \rho_0 S_{p,NMR,O} (\gamma_1 \gamma_5 h)^2 S(S+1) \sqrt{\tau_{m,O} \cdot \tau_{s,O}}} \cdot \\ \left[ 1 + \frac{3 \sqrt{2}}{8} \frac{\sqrt{1 + \sqrt{1 + \omega_1^2 \tau_{s,O}^2}}}}{\sqrt{1 + \omega_1^2 \tau_{s,O}^2}}} + \frac{13 \sqrt{2}}{8} \frac{\sqrt{1 + \sqrt{1 + \omega_5^2 \tau_{s,O}^2}}}}{\sqrt{1 + \omega_5^2 \tau_{s,O}^2}} \right] \end{cases}$$

where d and R are two parameters related to the pore size from modified Korb's model.  $\delta_{\rm W}$  and  $\delta_{\rm O}$  are the distances of closet approach of hydrogen protons within water and oil to paramagnetic ions on 2-D and 1-D pore surfaces.  $\rho_{\rm O}$  and  $\rho_{\rm W}$  represent the densities for oil and water.  $S_{\rm p,NMR,O}$  and  $S_{\rm p,NMR,W}$  represent the specific surface areas for OP and IP.  $\tau_{\rm s,w}$  and  $\tau_{\rm m,w}$  represent the surface residence and translational correlation times from water.  $\tau_{\rm m,o}$  and  $\tau_{\rm s,o}$  represent the translational and surface residence correlation times from oil.  $\gamma_{\rm I}$  and  $\omega_{\rm I}$  are the magnetic moment and angular frequency of  $^{1}{\rm H}$ , respectively.  $\gamma_{\rm S}$  and  $\omega_{\rm S}$  are the magnetic moment and angular frequency of paramagnetic ions near pore surfaces.  $\mu_{\rm O}$  is the vacuum permeability; h is the reduced Planck's constant.

Similar to the study of Korb et al., we assume that pores are cylindrical (Korb et al., 1999). The longitudinal surface relaxivity of water ( $\rho_{1S,W}$ ), longitudinal surface relaxivity of oil ( $\rho_{1S,O}$ ), transverse surface relaxivity of water ( $\rho_{2S,W}$ ), and transverse surface relaxivity of oil ( $\rho_{2S,O}$ ) exhibited frequency dependence, may be expressed as

#### 2.2. Simulation method based on $T_1$ - $T_2$

On the basis of the NMR  $T_1$ - $T_2$  relaxation theory proposed herein,  $T_1$ - $T_2$  responses were numerically simulated and experimentally measured, and the accuracy of the proposed relaxation theory was verified through  $T_1$ - $T_2$  experiments. The Inversion-recovery (IR)-Carr-Purcell-Meiboom-Gill (CPMG) allows the magnetization to vary over a wide range. It is shown in Fig. 1. It can be seen that this pulse sequence consists of two parts. The IR pulse is mainly used to edit  $T_1$ , while the CPMG pulse is used to measure  $T_2$ .

Echo data can be obtained by editing  $T_W$  during the measurement process. The collected echo data can be expressed as

$$Echo(T_{W},t) = \iint K_{1}(T_{W},T_{1})f(T_{1},T_{2})K_{2}(t,T_{2})dT_{1}dT_{2} + Noise(T_{W},t)$$
(6)

where  $K_1(T_W, T_1) = \left[1 - 2 \cdot \exp\left(-\frac{T_W}{T_1}\right)\right]$  and  $K_2(t, T_2) = \exp\left(-\frac{t}{T_2}\right)$  are the kernel function related to  $T_1$  and  $T_2$ , respectively.

$$\begin{cases} \rho_{1S,W} = \left(\frac{\mu_{0}}{4\pi}\right)^{2} \cdot \pi \bigg/ \left(60\delta_{W}^{2}\right) \cdot \sigma_{s,W} \rho_{W} S_{p,NMR,W}(\gamma_{1}\gamma_{s}h)^{2} S(S+1) \tau_{m,W} \cdot \\ \left[ 3 \ln \left(\frac{1 + \omega_{1}^{2} \tau_{m,W}^{2}}{\left(\frac{\tau_{m,W}}{\tau_{s,W}}\right)^{2} + \omega_{1}^{2} 2 \tau_{m,W}^{2}}\right) + 7 \ln \left(\frac{1 + \omega_{s}^{2} \tau_{m,W}^{2}}{\left(\frac{\tau_{m,W}}{\tau_{s,W}}\right)^{2} + \omega_{s}^{2} 2 \tau_{m,W}^{2}}\right) \right] \\ \rho_{2S,W} = \left(\frac{\mu_{0}}{4\pi}\right)^{2} \cdot \pi \bigg/ \left(30\delta_{W}^{2}\right) \cdot \sigma_{s,W} \rho_{W} S_{p,NMR,W}(\gamma_{1}\gamma_{s}h)^{2} S(S+1) \tau_{m,W} \cdot \\ \left[ 2 \ln \left(\frac{\tau_{s,W}}{\tau_{m,W}}\right)^{2} + \frac{3}{4} \ln \left(\frac{1 + \omega_{1}^{2} \tau_{m,W}^{2}}{\left(\frac{\tau_{m,W}}{\tau_{s,W}}\right)^{2} + \omega_{1}^{2} 2 \tau_{m,W}^{2}}\right) + \frac{13}{4} \ln \left(\frac{1 + \omega_{s}^{2} \tau_{m,W}^{2}}{\left(\frac{\tau_{m,W}}{\tau_{s,W}}\right)^{2} + \omega_{s}^{2} 2 \tau_{m,W}^{2}}\right) \right] \\ \rho_{1S,O} = \left(\frac{\mu_{0}}{4\pi}\right)^{2} \cdot \sqrt{2} \bigg/ \left(30\pi\delta_{0}^{2}\right) \cdot \sigma_{s,O} \rho_{O} S_{p,NMR,O}(\gamma_{1}\gamma_{s}h)^{2} S(S+1) \sqrt{\tau_{m,O} \cdot \tau_{s,O}} \cdot \\ \left[ \frac{3\sqrt{1 + \sqrt{1 + \omega_{1}^{2} \tau_{s,O}^{2}}}}{\sqrt{1 + \omega_{1}^{2} \tau_{s,O}^{2}}} + \frac{7\sqrt{1 + \sqrt{1 + \omega_{s}^{2} \tau_{s,O}^{2}}}}{\sqrt{1 + \omega_{s}^{2} \tau_{s,O}^{2}}} \right] \\ \rho_{2S,O} = \left(\frac{\mu_{0}}{4\pi}\right)^{2} \cdot 1 \bigg/ \left(15\pi\delta_{0}^{2}\right) \cdot \sigma_{s,O} \rho_{O} S_{p,NMR,O}(\gamma_{1}\gamma_{s}h)^{2} S(S+1) \sqrt{\tau_{m,O} \cdot \tau_{s,O}} \cdot \\ \left[ 1 + \frac{3\sqrt{2}}{8} \frac{\sqrt{1 + \sqrt{1 + \omega_{1}^{2} \tau_{s,O}^{2}}}}{\sqrt{1 + \omega_{1}^{2} \tau_{s,O}^{2}}} + \frac{13\sqrt{2}}{8} \frac{\sqrt{1 + \sqrt{1 + \omega_{s}^{2} \tau_{s,O}^{2}}}}{\sqrt{1 + \omega_{s}^{2} \tau_{s,O}^{2}}} \right] \end{aligned}$$

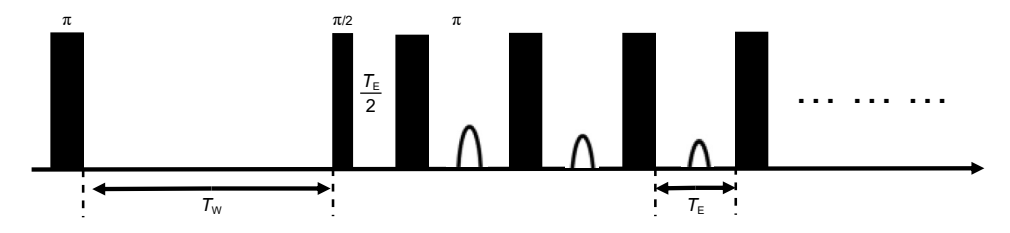


Fig. 1. Schematic diagram of the IR-CPMG pulse sequence.

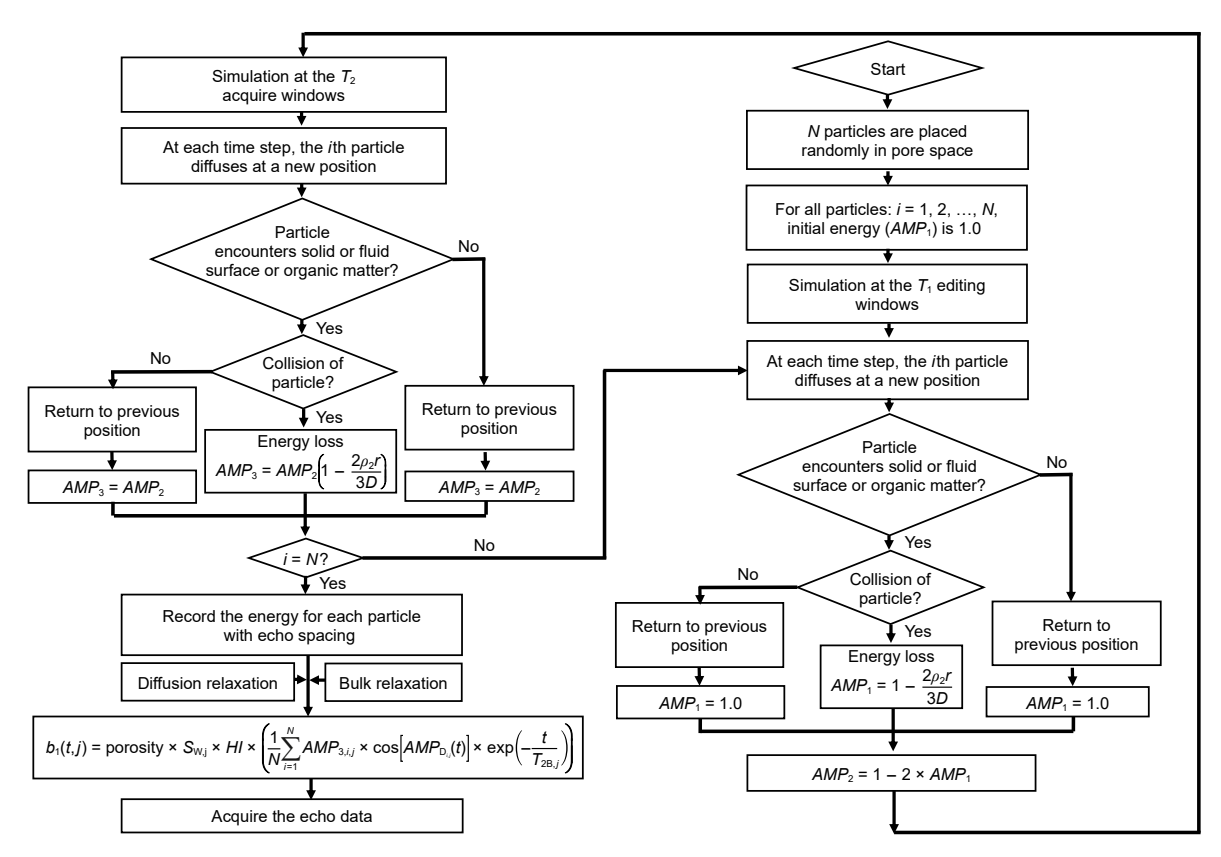


Fig. 2. Flow diagram for numerical simulation with the IRW algorithm.

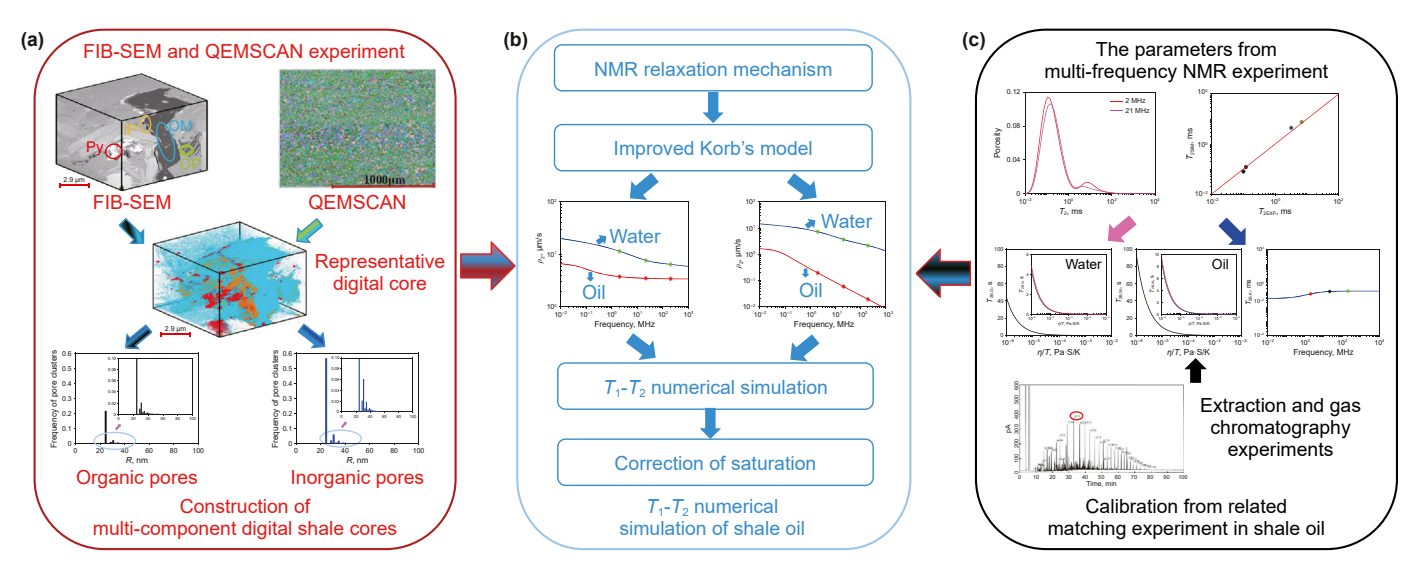


Fig. 3. Experimental processes and parameters determination.

 $Noise(T_{W}, t)$  is the noise in the measurement.

Random walk algorithms have been used in the numerical study for sandstones (Guo et al., 2020; Guo and Xie, 2019). Considering the uneven pore size distribution in shale oil reservoirs, the IRW algorithm was proposed on the basis of the previously constructed multi-component digital shale cores (Liu et al., 2023, 2024c) for the first time. Different from previous NMR numerical simulations in sandstone, in the  $T_1$  editing window, the proposed method was used to simulate each hydrogen nucleus underwent a random walk

process, during which if the nucleus encountered OM or mineral, its energy decayed. Subsequently, the inversion recovery pulse was added. In the  $T_2$  collection window, hydrogen nucleus continued its random walk. When it encountered OM or mineral, its energy decayed. Meanwhile, the energy of each hydrogen nucleus decayed due to diffusion relaxation, and it was counted statistically. Finally, the energy values of all hydrogen nuclei for each echo were added.

The detailed simulation process was shown in Fig. 2.

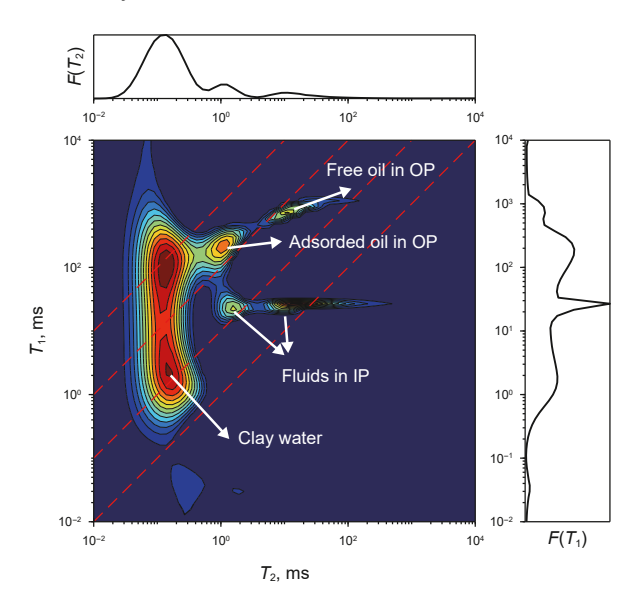


Fig. 4. Experimental results of the shale sample.

**Table 1**Transverse and longitudinal relaxivities at different magnetic field frequencies.

Surface relaxivities, μm/s	Fluid types	Surface relaxivities at different frequencies, μm/s		
		2 MHz	21.36 MHz	200 MHz
$ ho_{2S}$	Oil	3.8	3.5	3.4
	Water	11.5	7.65	6.13
$ ho_{1S}$	Oil	0.2	0.06	0.02
	Water	9.8	3.7	2.9

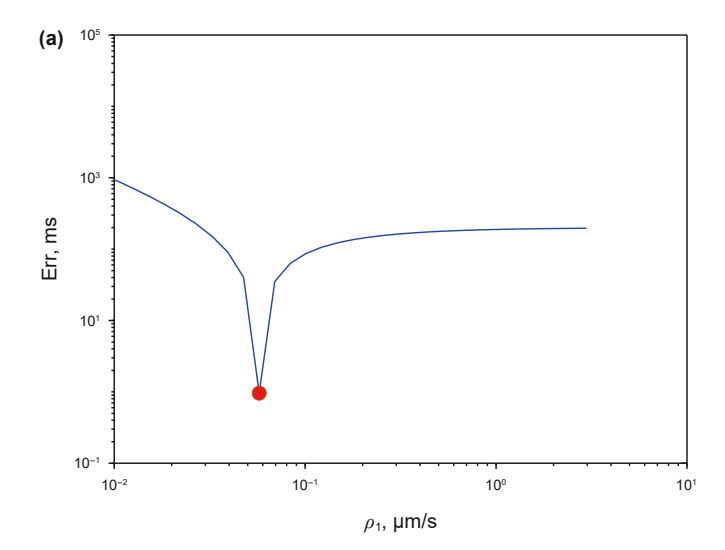
#### 3. Experimental

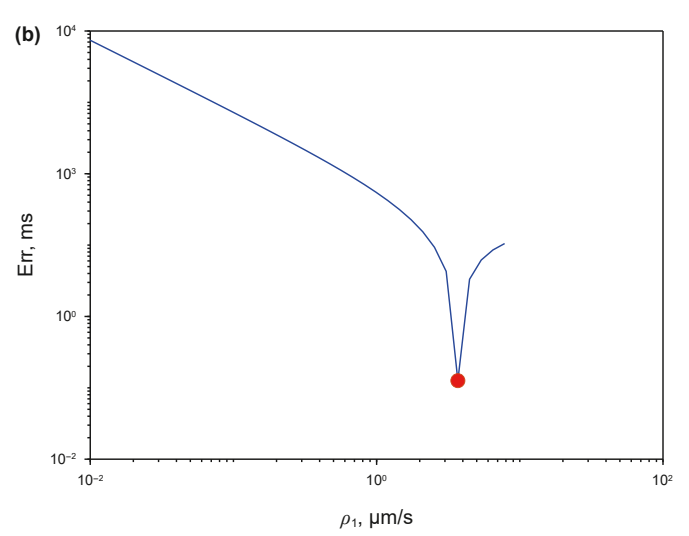
#### 3.1. Research plans and ideas

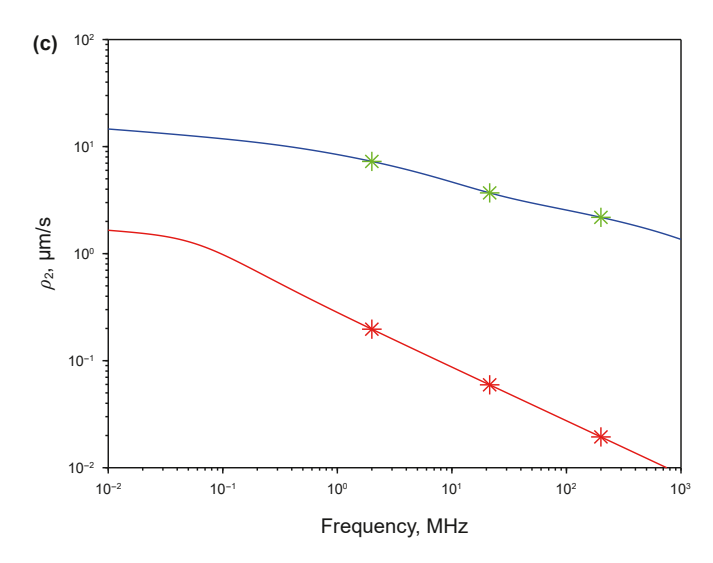
The experimental part is the verification of this study. Fig. 3 shows the research ideas on the basis of experiments. We have created multi-component digital shale cores on the basis of FIB-SEM and quantitative evaluation of minerals by scanning electron microscopy (QEMSCAN) (Liu et al., 2023) (Fig. 3(a)). Through different frequencies (2 MHz and 21.36 MHz) NMR, extraction and GC experiments (Fig. 3(c)), the  $T_{2B,O}$ ,  $T_{2B,W}$ , and  $T_{2B,K}$  of shale oil were determined (Liu et al., 2024c). Then one parallel sample can be conducted on IR-CPMG experiment in Section 3.1, and the  $T_1$ - $T_2$ spectra can be acquired through inversion. In Section 3.2, the  $\rho_{\rm 1S,O}$ and  $\rho_{1S,W}$  would be determined through Eqs. (1)–(5) combined with IR-CPMG experiments. The accuracy of the  $T_1$ - $T_2$  relaxation theory could be verified. These works provided foundations for subsequent numerical investigations on the basis of  $T_1$ - $T_2$  relaxation theory and frequency conversion for the saturations of various components (Fig. 3(b)).

#### 3.2. IR-CPMG experiment

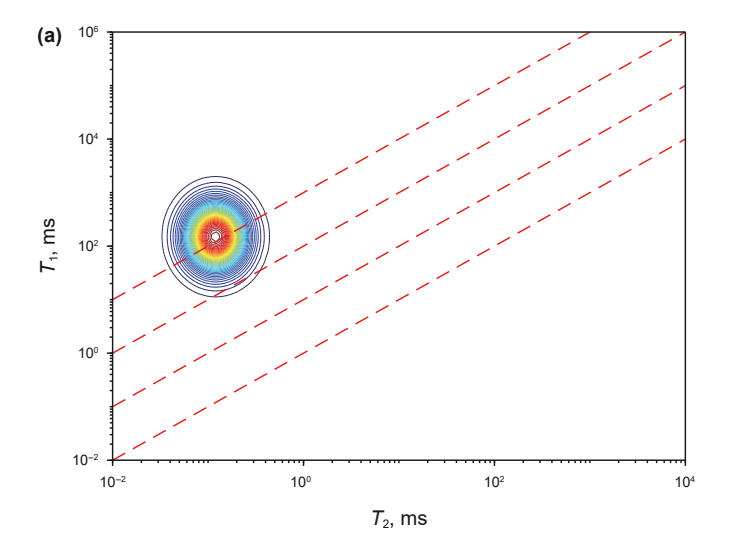
A high-field NMR experiment was conducted on a shale sample (Sample #AA-2) using an NMR core analyzer (MesoMR23-060H-I, Niumag, China) with a 21.36 MHz frequency. The shale sample was measured by the IR-CPMG pulse sequence. During the measurement process,  $T_{\rm E}$  is 0.08 ms, number of echoes (also known as echo train length) is 2000, and the ambient temperature is 25 °C. After the measurement was completed, the  $T_1$ - $T_2$  spectra of sample #AA-

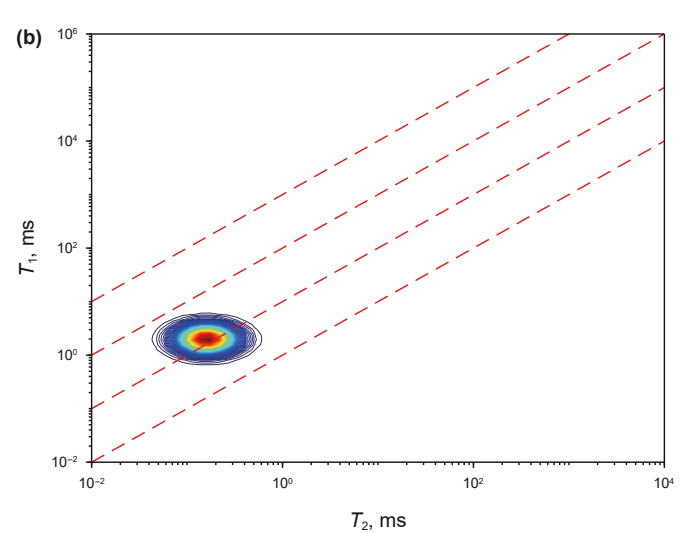






**Fig. 5.** Calibration of experimental parameters. In Fig. 5(a)–(b), the blue solid lines represent the variation of the error (Err) between the  $T_1$  of numerical simulation and the experimental results as the function of  $\rho_{1S,O}$  or  $\rho_{1S,W}$  ( $\rho_1$ ), and red solid dot are the optimal  $\rho_{1S,O}$  or  $\rho_{1S,W}$ , respectively. In Fig. 5(c), the red and blue solid lines are the varying  $\rho_{1S,O}$ ,  $\rho_{1S,W}$ .





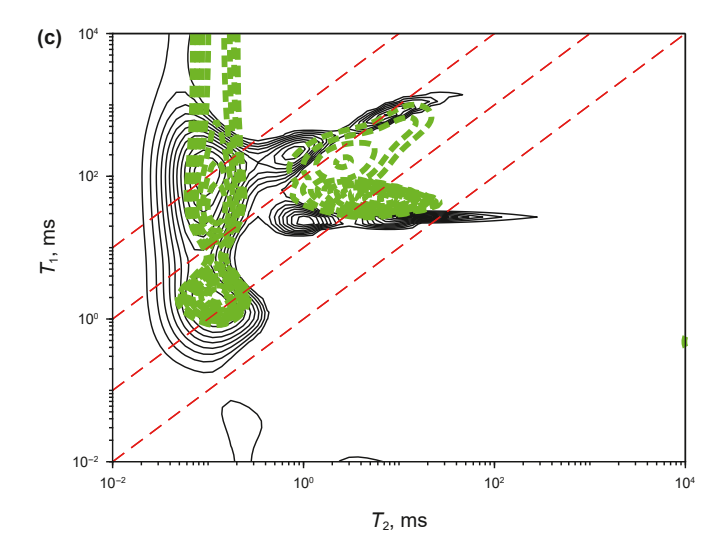


**Fig. 6.** Comparison of numerical investigations and experimental results. **(a)**  $T_1$ - $T_2$  spectrum of organic matter; **(b)**  $T_1$ - $T_2$  spectrum of clay-bound water; **(c)** comparison from the numerical and experimental  $T_1$ - $T_2$  spectrum at the frequency of 21.36 MHz, and the green dotted line represents the  $T_1$ - $T_2$  spectrum obtained from numerical simulations on the basis of digital core.

2 were obtained through Butler-Reeds-Dawson (BRD) inversion method (Butler et al., 1981). The distributions of the signals for various components on the  $T_1$ - $T_2$  spectra were shown in Fig. 4. In Fig. 4, the signals for OM show a high  $T_1$  value, a low  $T_2$  value, and a high  $T_1/T_2$  value, while the signals for adsorbed oil (OP oil during simulation) show a high  $T_1$  value, a relatively low  $T_2$  value, and a high  $T_1/T_2$  value, and the signals for clay-bound water and IP water show low  $T_1$ ,  $T_2$  and  $T_1/T_2$  values. The results are consistent with the study from Li et al., which verifies the reasonability of the results (Li et al., 2020). It is noted that the #AA-2 has been previously used for NMR experiments with different frequencies. Therefore, the results of the high-field NMR experiment and the previous NMR experiments with different frequencies can be used to determine the  $\rho_{15,0}$ ,  $\rho_{15,W}$ ,  $\rho_{25,0}$ , and  $\rho_{25,W}$ .

### 3.3. Parameters determination and results verification

#### 3.3.1. Parameters calibration

On the basis of improved Korb's theory, the  $\rho_{1S,O}$ ,  $\rho_{1S,W}$ ,  $\rho_{2S,O}$ , and  $\rho_{2S,W}$ .at 2, 21.36, and 200 MHz were determined. The results were given in Table 1. Since distributions of fluids and minerals in the shale sample remained unchanged, the determined parameters previously were unchanged.

The  $\rho_{1S,O}$ , and  $\rho_{1S,W}$  were calibrated by the IR-CPMG (Fig. (5)). It can be seen from Fig. 5(a) that the  $\rho_{1S,O}$  at 21.36 MHz is 0.06 µm/s, while the error of  $T_1$  measurement is 6.9 ms, and the corresponding value of  $\tau_s$  is 1.37 µs, which is just a bit above 0.78 µs determined by Korb et al (2014). As shown in Fig. 5(b), the determined  $\rho_{1S,W}$  at 21.36 MHz is 3.7 µm/s, while the error of  $T_1$  measurement is 0.13 ms, and the corresponding value of is 0.1 µs, which is close to 0.6 µs determined by Korb et al. The results above verify the reasonability of related parameters. In the meanwhile, the  $\rho_{1S,O}$ ,  $\rho_{1S,W}$ ,  $\rho_{2S,O}$  and  $\rho_{2S,W}$  were also determined (Table 1). Based on the results of Fig. 5(a) and (b) as well as Eqs. (4) and (5), Frequency conversion equations were determined (Fig. 5(c)). It can be utilized to lay the foundation for subsequent numerical investigations.

#### 3.3.2. Results verification

The  $T_{1K}$  and  $T_{2K}$  can be determined according to the P model (Eq. (2)). The values for  $T_{2B, K}$  at 2, 21.36, and 200 MHz determined on the basis of the P model were 80, 120, and 130 μs, respectively. The values for  $T_{1B, K}$  at these frequencies were 17, 150, and 1355 ms. Fig. 6(a) shows the  $T_1$ - $T_2$  spectra of OM at 21.36 MHz. Assuming that the signal of clay-bound water does not change with magnetic field frequency, the  $T_1$ - $T_2$  spectra of clay-bound water were regarded as a Gaussian spectra with transverse bulk relaxation time  $(T_{2B,CL})$  of 0.12 ms and longitudinal bulk relaxation time ( $T_{\rm 1B,CL}$ ) of 1.5 ms. To verify the accuracy of  $T_1$ - $T_2$  simulation, the  $T_1$ - $T_2$  spectra of OM, clay-bound water, IP water, and OP oil obtained through the simulation of digital cores were compared with that from the experimental measurements at 21.36 MHz. The results show that the peaks of the  $T_1$ - $T_2$  spectra of OM, clay-bound water, and OP oil, and IP water obtained from numerical simulations were highly consistent with those from experimental measurements, which verified the accuracy of NMR  $T_1$ - $T_2$  relaxation theory. In addition, the  $\rho_{1S,O}$ ,  $\rho_{1S,W}$ ,  $\rho_{2S,O}$ , and  $\rho_{2S,W}$  from experiments can be used for subsequent numerical investigations. It is noted that if the echo of OP oil and IP water were inverted together, the results of coupled inversion would be displayed, making it impossible to compare the peak positions of  $T_1$ - $T_2$  spectra from experiment and numerical simulation. The reason is that the signal of oil was weaker than that of water. Therefore, the intensity of the signal of oil in the  $T_1$ - $T_2$ spectrum obtained from numerical investigations was amplified 5 times.

The accuracy of the numerical simulations on the basis of an

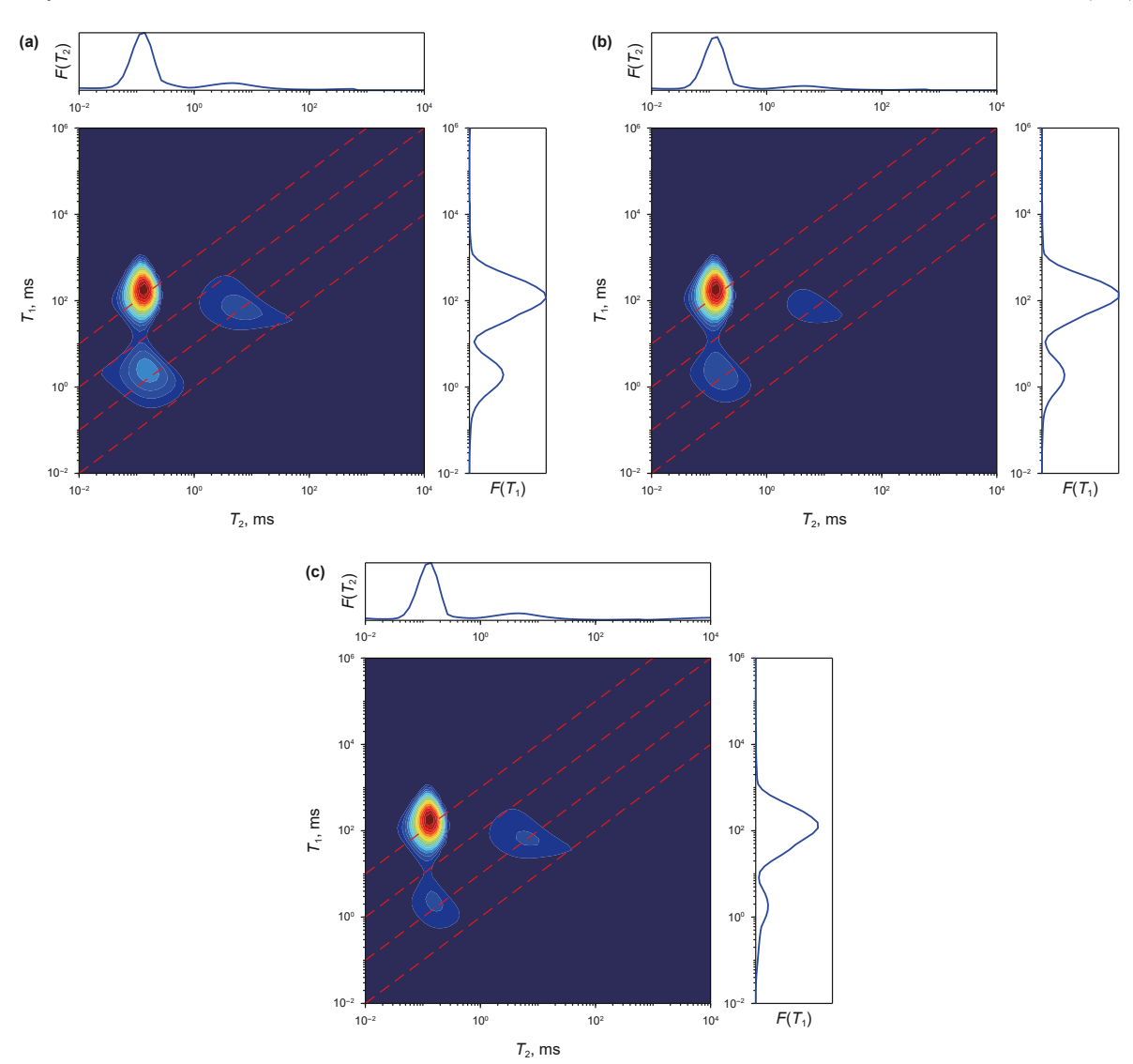


**Fig. 7.** Results for the  $T_1$ - $T_2$  responses of organic matter with different HI values at the frequency of 21.36 MHz. Fig. 7(a), (b) and (c) show the  $T_1$ - $T_2$  spectra of organic matter with HI values of 0.3, 0.5, and 0.7.

IRW algorithm and the NMR  $T_1$ - $T_2$  relaxation theory has been verified in chapter 3.2. Since it is difficult to describe the effect of a single factor on  $T_1$ - $T_2$  responses in shale oil reservoirs, the effect of each factor was quantified from numerical simulations to provide a foundation for the subsequent saturation frequency conversion for each component. The multi-component digital shale cores in this study are varying pyrite contents (0.55%, 1.77%, 2.68%, 3.94%, 5.3%, 6.9%), clay contents (0%, 1.03%, 3.39%, 5.12%, 10.49%, 20.14%) and types of clay mineral (Liu et al., 2024c).

## 4. Numerical simulation

#### 4.1. Hydrogen index (HI) of OM

The HI of OM affects the determination of fluid component saturations for the  $T_1$ - $T_2$  spectra. The  $T_1$ - $T_2$  spectra for OM with varying HI were shown in Fig. 7. In Fig. 7, the signal intensity for OM increases with the increased HI of OM, while the signal intensities of clay-bound water, OP oil, and IP water decreases with the increased HI of OM.

#### 4.2. Pyrite content

On the basis of the  $T_1$ - $T_2$  relaxation theory and the previously constructed multi-component digital shale cores with varying pyrite contents (Liu et al., 2024c), the IR-CPMG was simulated using the IRW algorithm. The  $T_1$ - $T_2$  spectra of all components (OM, claybound water, oil, and water) with varying frequencies, pyrite contents and  $T_E$  were obtained from BRD inversion (as shown in Fig. 8(a)–(i)). The results show that, as the magnetic field frequency enhances and other parameters are unchangeable, the peaks of the  $T_1$ - $T_2$  spectra of OM shift toward the upper right corner because the  $T_{1B,K}$  and  $T_{2B,K}$  increased with the increased magnetic field frequency.  $T_{1B,K}$  are more dependent on frequency than  $T_{2B,K}$ . Therefore, the peaks of the  $T_1$  spectra of OM shift to a larger extent than the  $T_2$  spectra. When pyrite content increases and other parameters are unchangeable, the peaks of the  $T_2$  and  $T_1$  spectra of OM and clay-bound water do not shift because pyrite content only have a minor impact on the  $T_{2B,K}$  and  $T_{2B,CL}$ . The results show that, when magnetic field frequency is 2 MHz and pyrite content is low,  $T_2$  and  $T_1$  do not change with pyrite content (Fig. 8(a), (d) and (g)). When pyrite content is high, the peaks of the  $T_2$  spectra shift toward the

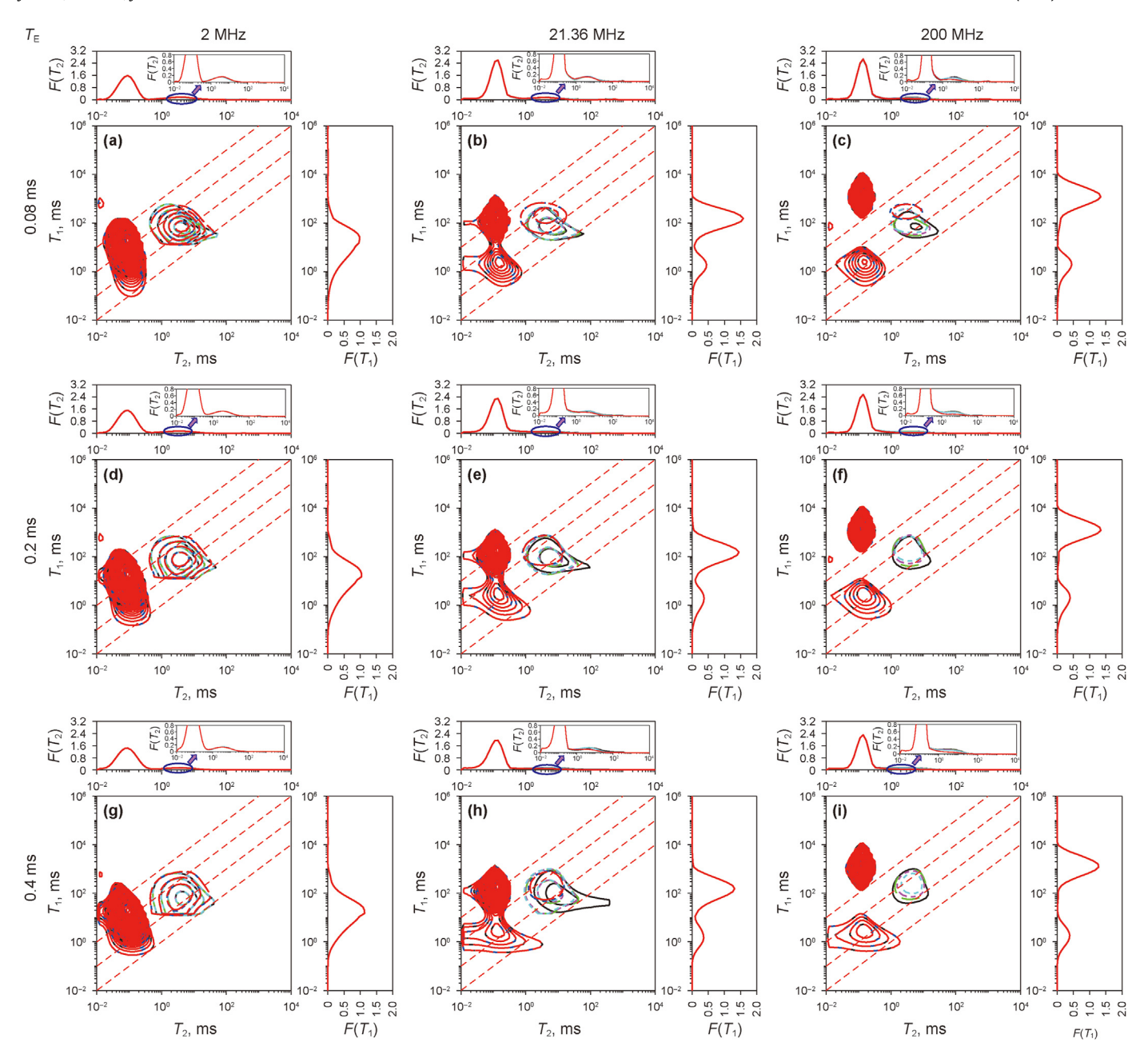


**Fig. 8.**  $T_1$ - $T_2$  spectra of various fluids at different magnetic field frequencies with varying  $T_E$  and pyrite contents. The black, green, purple, cyan, blue and red lines are the  $T_1$ - $T_2$  spectra for various fluids with varying pyrite contents (0.55%, 1.77%, 2.68%, 3.94%, 5.3%, and 6.9%).

direction of the short relaxation component as pyrite content increases (Fig. 8(a), (d) and (g)), while  $T_1$  do not change significantly. When magnetic field frequency is 2 MHz and pyrite content is low, the fluid mainly undergoes surface relaxation, while bulk relaxation and diffusion relaxation are negligible. However, because diffusion relaxation cannot be neglected when pyrite content is high, the peaks of  $T_2$  spectra shift toward the direction of the short relaxation component as pyrite content increases. The peaks of  $T_2$  spectra shift toward the direction of the short relaxation component, and the spectral intensity decreases as pyrite content increases at 21.36 and 200 MHz frequencies (Fig. 8(b)–(c), (e)–(f), and (h)–(i)). Under the aforementioned conditions, the fluid is subject to the combined effects of surface relaxation and diffusion relaxation. As pyrite content increases, the magnetic susceptibility difference between the shale matrix and the fluid increases, and the

internal magnetic field gradient increases, relaxation rates accelerated due to the enhanced diffusion relaxation. Therefore, the peaks of the  $T_2$  spectra shift to the left, and the spectral intensities decrease. When other conditions remain unchanged, an increased  $T_{\rm E}$  would, on the one hand, reduce the instrument's ability to detect hydrogen signals and reduce the intensities of the signals of various components. On the other hand, it would enhance diffusion relaxation and accelerate echo, resulting in sparse signal contours and reduced spectral intensity (Fig. 8(a), (d), (g); Fig. 8(b), (e), (h); Fig. 8(c), (f), (i)). It should be noted that, when pyrite content is very high, enhanced diffusion relaxation can result in excessively low intensity of some  $T_1$ - $T_2$  spectra, making it difficult to observe changes in contours in the  $T_1$ - $T_2$  spectra (Fig. 8(e)–(f) and Fig. 8(h)–(i)).

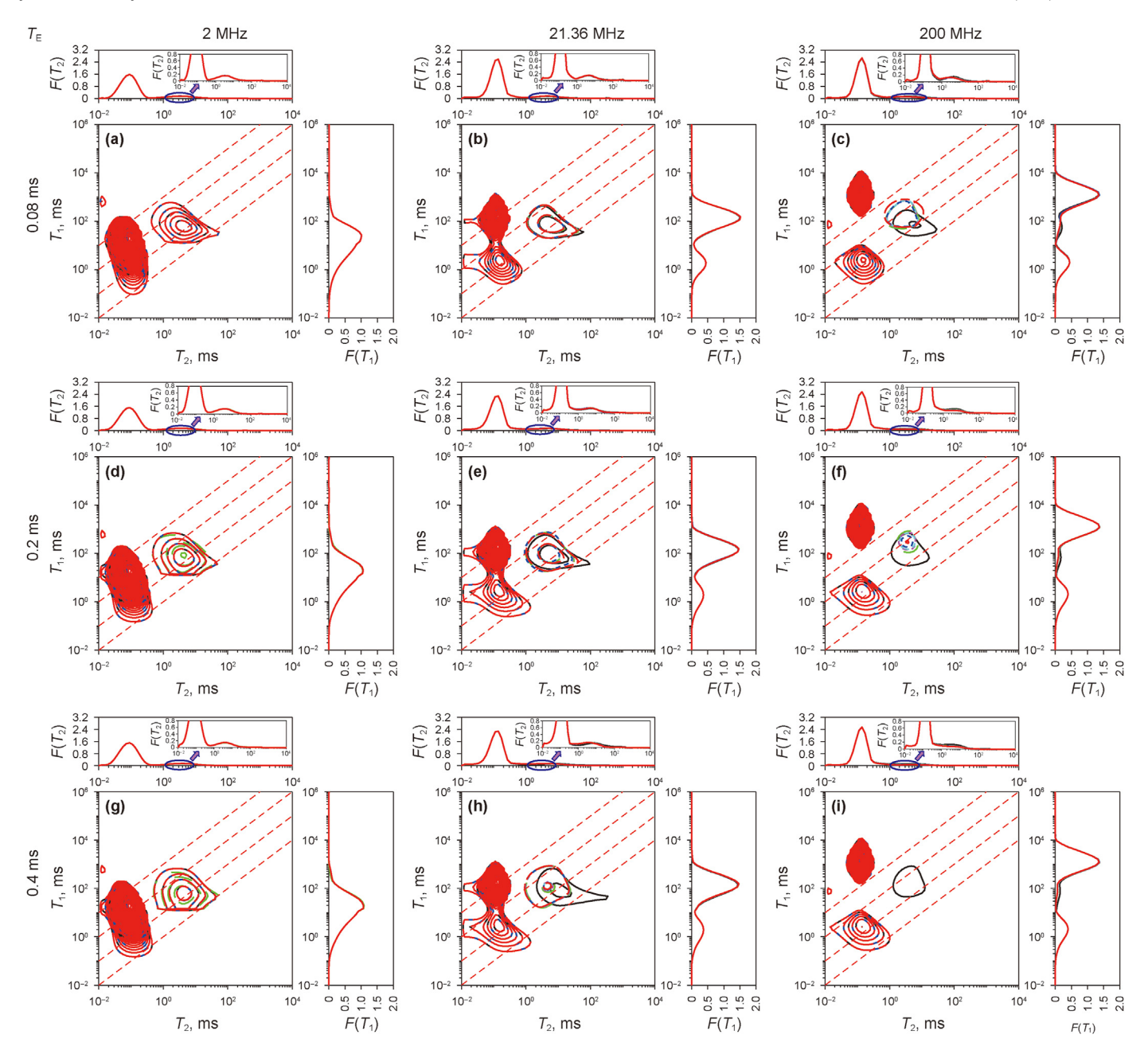


**Fig. 9.**  $T_1$ - $T_2$  spectra of various fluids at different magnetic fields frequencies with varying  $T_E$  and clay contents. The black line, green line, purple line, cyan line, blue line and red line represent the  $T_1$ - $T_2$  spectra of various fluids under conditions of varying clay content (0%, 1.03%, 3.39%, 5.12%, 10.49%, and 20.14%).

## 4.3. Clay content

On the basis of the  $T_1$ - $T_2$  relaxation theory and the previously constructed multi-component digital shale cores with varying clay content (Liu et al., 2024c), the IR-CPMG was simulated using the IRW algorithm. The  $T_1$ - $T_2$  spectra of all components with varying frequency,  $T_E$  and clay content were obtained from BRD inversion (as shown in Fig. 9(a)—(i)). The results show that, as magnetic field frequency increases while other parameters are unchangeable, the peaks of the  $T_1$ - $T_2$  spectra of OM shift toward the upper right corner. As clay content increases while other parameters are unchangeable, the peaks of the  $T_2$  and  $T_1$  spectra of OM and clay-bound water do not shift. We would not be explained repeatedly here because it has already been explained in the previous section. The results also show that, when magnetic field frequency is 2 MHz,  $T_2$  and  $T_1$  do

not change with clay content (Fig. 9(a), (d), (g)), and  $T_1$  does not change significantly. When magnetic field frequency is 2 MHz, the fluid mainly undergoes surface relaxation, and bulk relaxation and diffusion relaxation are negligible. The  $T_2$  spectra peak shift toward the direction of the short relaxation component, and the spectral intensity decreases as clay content increases at 21.36 and 200 MHz frequencies (Fig. 9(b)–(c), (e)–(f) and (h)–(i)), and  $T_1$  does not change significantly. Because under the aforementioned conditions, the fluid was subject to the combined effects of surface relaxation and diffusion relaxation. As clay content increased, the magnetic susceptibility difference between the shale matrix and the fluid increased, and the internal magnetic field gradient increased, resulting in enhanced diffusion relaxation and accelerated echo. Therefore, the peaks of the  $T_2$  spectra shifted to the left, and the spectral intensity decreased. When other conditions

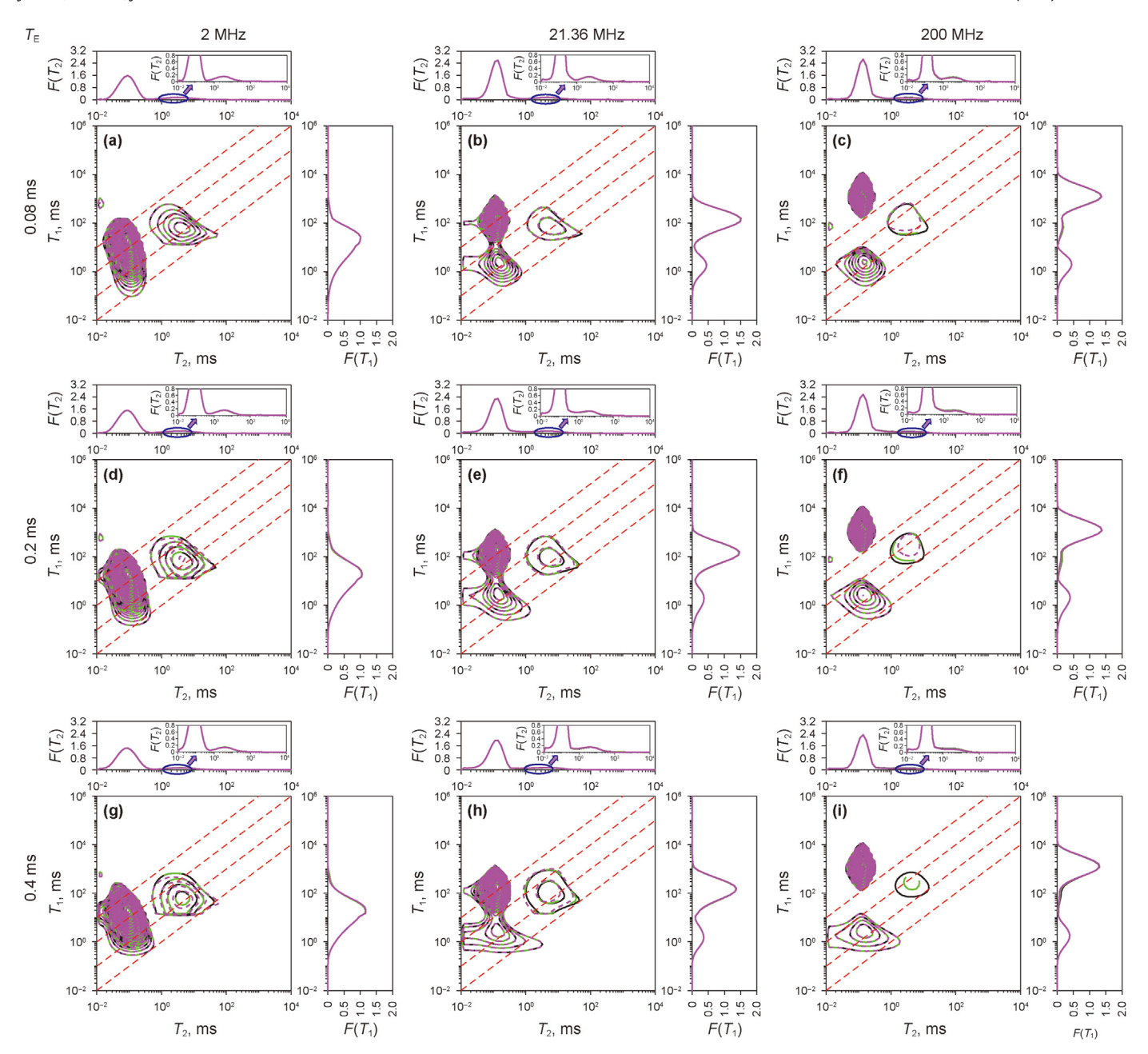


**Fig. 10.**  $T_1$ - $T_2$  spectra of various fluids at different magnetic fields frequencies with varying  $T_E$  and different types of clay mineral. The black, green and purple lines represent the  $T_1$ - $T_2$  spectra of various fluids involving different types of clay mineral (M, ILL, CH).

remain unchanged, an increase in  $T_{\rm E}$  would, on the one hand, reduce the instrument's ability to detect hydrogen signals and reduce the intensities of the signals of various components. On the other hand, it would enhance diffusion relaxation and accelerate relaxation rates, resulting in sparse signal contours and reduced spectral intensity (Fig. 9(a), (d), (g), (b), (e), (h), and (c), (f), (i)). It is to be noted that, when clay content is high and magnetic field frequency is very high, enhanced diffusion relaxation can result in excessively low intensities of some  $T_1$ - $T_2$  spectra, making it difficult to observe changes in contours in the  $T_1$ - $T_2$  spectra (Fig. 9(f) and (i)).

#### 4.4. Clay mineral type

On the basis of the NMR relaxation theory and the previously constructed multi-component digital shale cores with different clay minerals (Liu et al., 2024c), the IR-CPMG was simulated using the IRW algorithm. The  $T_1$ - $T_2$  spectra of all components for different clay minerals were obtained from BRD inversion with varying frequencies and  $T_E$  (as shown in Fig. 10(a)—(i)). The results show that, as magnetic field frequency increases while other parameters are unchangeable, the peaks of the  $T_1$ - $T_2$  spectra of OM shift toward the upper right corner. As clay mineral type changes (the magnetic susceptibility increased) while other parameters are unchangeable, the peaks of the  $T_2$  and  $T_1$  spectra of OM and clay-bound water do not shift. The reason would not be explained repeatedly here because it has already been explained in the previous section. The results also showed that, when magnetic field frequency is 2 MHz,  $T_2$  and  $T_1$  do not change with clay mineral type (Fig. 10(a), (d), (g)), and  $T_1$  do not change significantly. When magnetic field frequency is 2 MHz, the fluid mainly underwent surface relaxation, and bulk

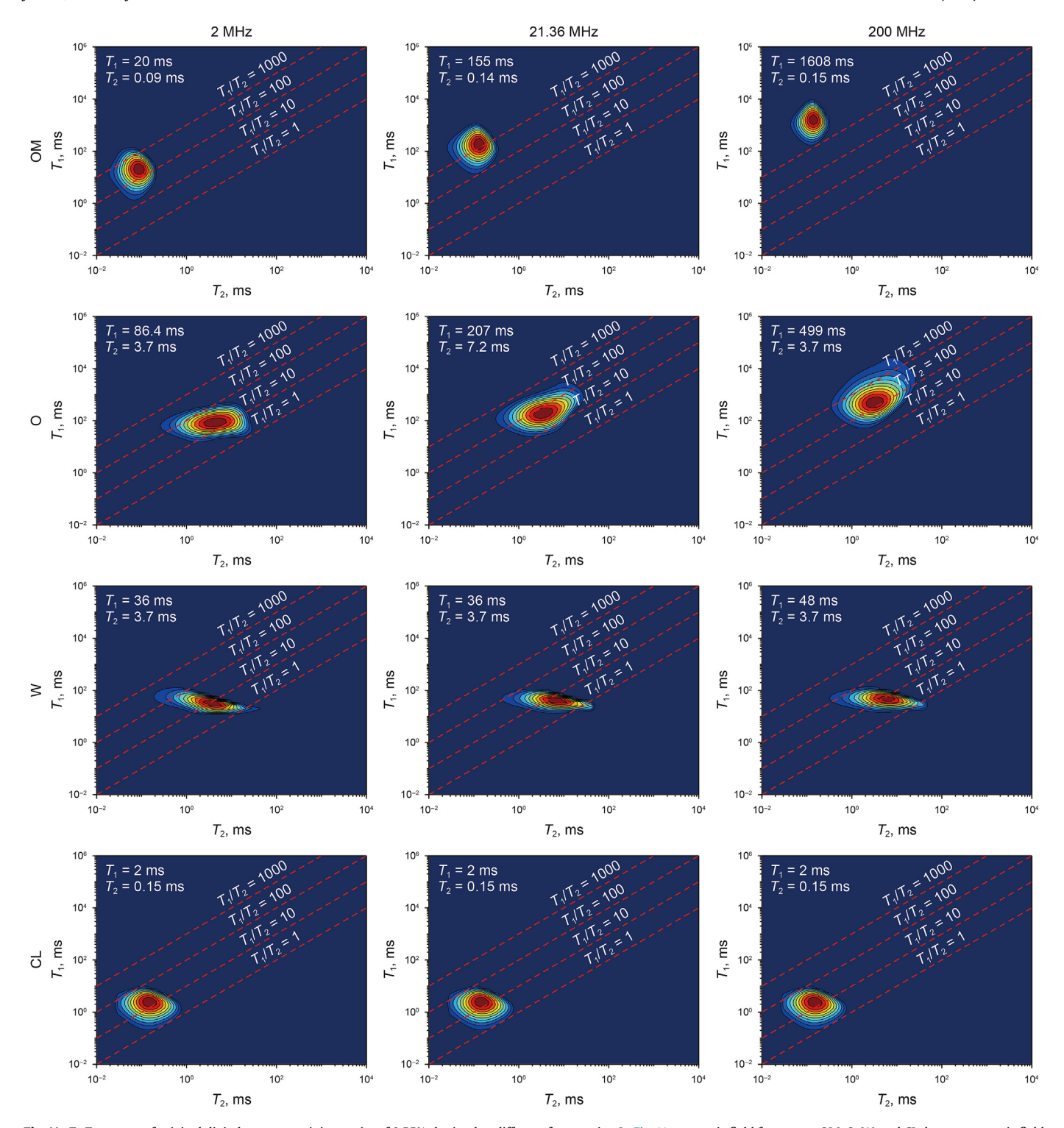


**Fig. 11.**  $T_1$ - $T_2$  spectra of original digital cores containing pyrite of 0.55% obtained at different frequencies. In Fig. 11, magnetic field frequency, OM, O, W, and CL denote magnetic field frequency, OM, oil, water, and clay-bound water, respectively.

relaxation and diffusion relaxation were negligible. For frequencies of 21.36 and 200 MHz, the  $T_2$  spectra peaks shift toward the direction of the short relaxation component as clay mineral type changed (the magnetic susceptibility increases), and the spectral intensity decreases (Fig. 10(b)-(c), (e)-(f) and 10(h)-(i)), and  $T_1$  does not change significantly. The reason is that, under the

aforementioned conditions, the fluid is subject to the combined effects of surface relaxation and diffusion relaxation. The magnetic susceptibility difference between the shale matrix and the fluid increased, and the internal magnetic field gradient increase as clay mineral type changes (the magnetic susceptibility increases), the relaxation rates accelerated due to the enhanced diffusion

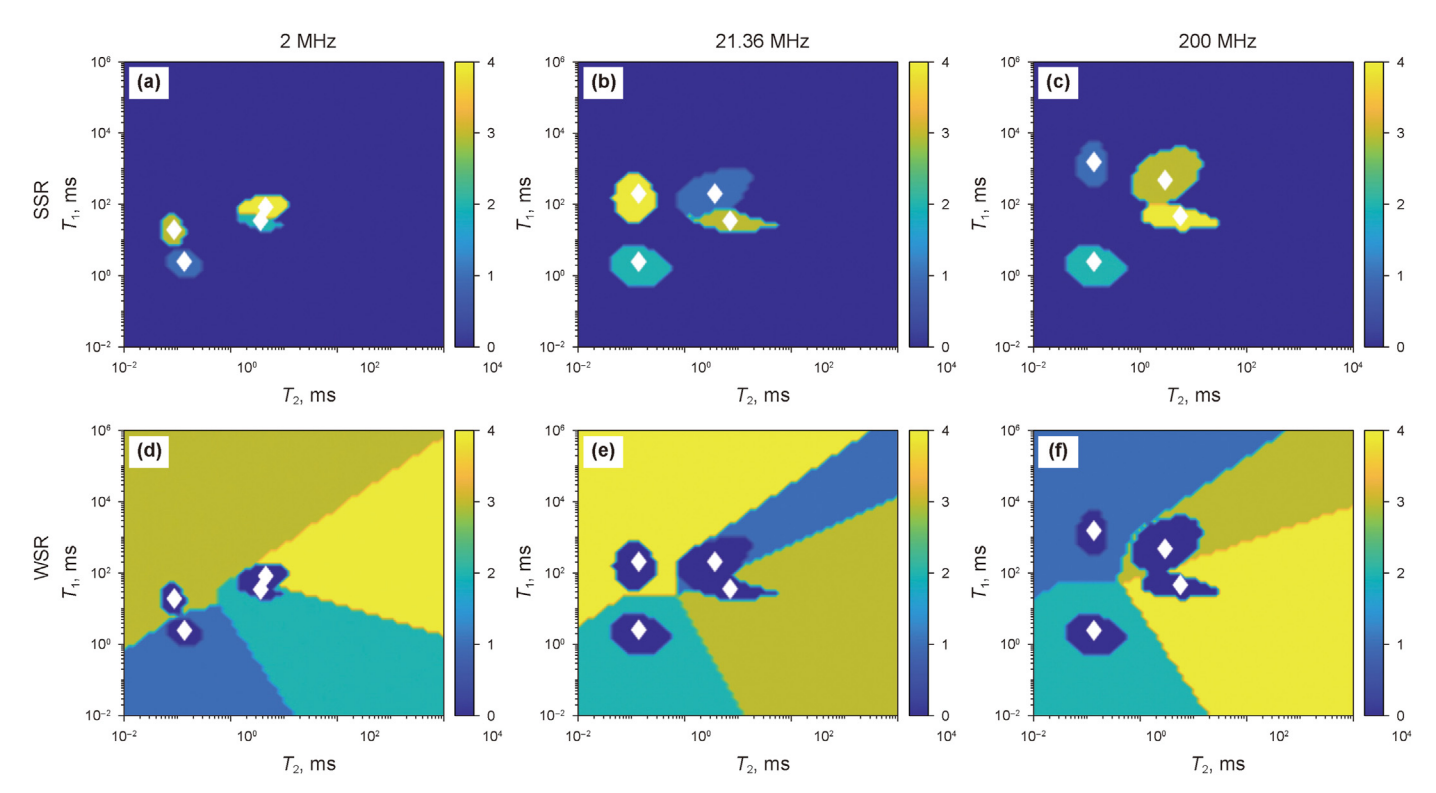


**Fig. 12.**  $T_1$ - $T_2$  spectra of original digital cores containing pyrite of 0.55% obtained at different frequencies. For the frequency of 2 MHz, the strong signal diagram (**a**) corresponds to the weak signal diagram (**d**); the dark yellow, yellow, green and blue zones represent OM, oil, water, and clay-bound water, respectively. For the frequency of 21.36 MHz, the strong signal diagram (**b**) corresponds to the weak signal diagram (**e**); the yellow, blue, dark yellow and green zones represent OM, oil, water, and clay-bound water, respectively. For the frequency of 200 MHz, the strong signal diagram (**c**) corresponds to the weak signal diagram (**f**); the blue, dark yellow, yellow and green zones represent OM, oil, water, and clay-bound water, respectively. SSR represents strong signal area and WSR represents weak signal area.

relaxation. Therefore, the peaks of the  $T_2$  spectra shift to the left, and the spectral intensity decreases. When other conditions remain unchanged, an increase in  $T_{\rm E}$  would, on the one hand, reduce the instrument's ability to detect hydrogen signals and reduce the intensities of the signals of various components. On the other hand, it would enhance diffusion relaxation and accelerate relaxation rates, resulting in sparse signal contours and reduced spectral intensity (Fig. 10(a), (d), (g), (b), (e), (h), and (c), (f), (i)). When the magnetic susceptibility of clay is high and magnetic field frequency is very high, enhanced diffusion relaxation can result in excessively low intensities of some  $T_1$ - $T_2$  spectra, making it difficult to observe changes in contours in the  $T_1$ - $T_2$  spectra (Fig. 10(f) and (i)).

# 5. Frequency conversion of petrophysical parameters

The effects of pyrite content, clay mineral type, and clay content on  $T_1$ - $T_2$  responses in shale oil reservoirs were analyzed from numerical simulations at 2, 21.36, and 200 MHz. Next step, we tried to accurately quantize the effects of various factors on petrophysical parameters such as saturation of each component.

Blind source separation (BSS) algorithms have been usually used for saturation calculation of fluid components in  $T_1$ - $T_2$  spectra (Gu et al., 2021). On the basis of the results of numerical simulations for original digital cores, the peak positions of various components in the  $T_1$ - $T_2$  spectra were determined. Blind source separation algorithms were performed for fluid signals in the  $T_1$ - $T_2$  spectra from 100 different porosity data, and the signals of OM, oil, water, and clay-bound water at 2, 21.36, and 200 MHz were obtained (Fig. 11). The results showed that the signals of various components were clear.

The signals shown in Fig. 11 were classified into strong and weak signals, and their distributions for various components were identified (as shown in Fig. 12). The results showed the strong and weak signals were clear (Fig. 12(a), (d), 12(b), (e), and 12(c), (f)). The BSS results obtained at different frequencies can be used to determine the saturation of various components with varying pyrite content, types of clay mineral, and clay content.

# 5.1. Petrophysical parameters frequency conversion for different pyrite contents

On the basis of the  $T_1$ - $T_2$  spectra shown in Fig. 12, the changes in OM saturation, Oil saturation ( $S_0$ ), IP water saturation ( $S_W$ ), and clay-bound water saturation ( $S_{CL}$ ) with varying magnetic field frequencies,  $T_E$  and pyrite contents were identified (Fig. 13(a)–(d)). As shown in Fig. 13(a), OM saturation increases and other parameters are unchangeable as magnetic field frequency increases. Due to the frequency dependence from OM, the  $T_{2B, K}$  and  $T_{1B, K}$  increased with the increased frequency. As  $T_{\rm E}$  increases and other parameters are unchangeable, OM saturation decreases with low pyrite content and increases with high pyrite content (Fig. 13(a)). For formations with high pyrite content, the significantly enhanced diffusion relaxation of pore fluids would cause the fluid signals to move to the position around OM in  $T_1$ - $T_2$  spectra. For formations with low pyrite content, the movement extents of fluid signals in  $T_1$ - $T_2$ spectra are low, and the increased  $T_{\rm E}$  would reduce intensities of the detected fluid signals. As shown in Fig. 13(b) and (c),  $S_0$  and  $S_W$ decrease as magnetic field frequency increases and other parameters are unchangeable. When magnetic field frequency increases, the significantly enhanced diffusion relaxation of pore fluids would

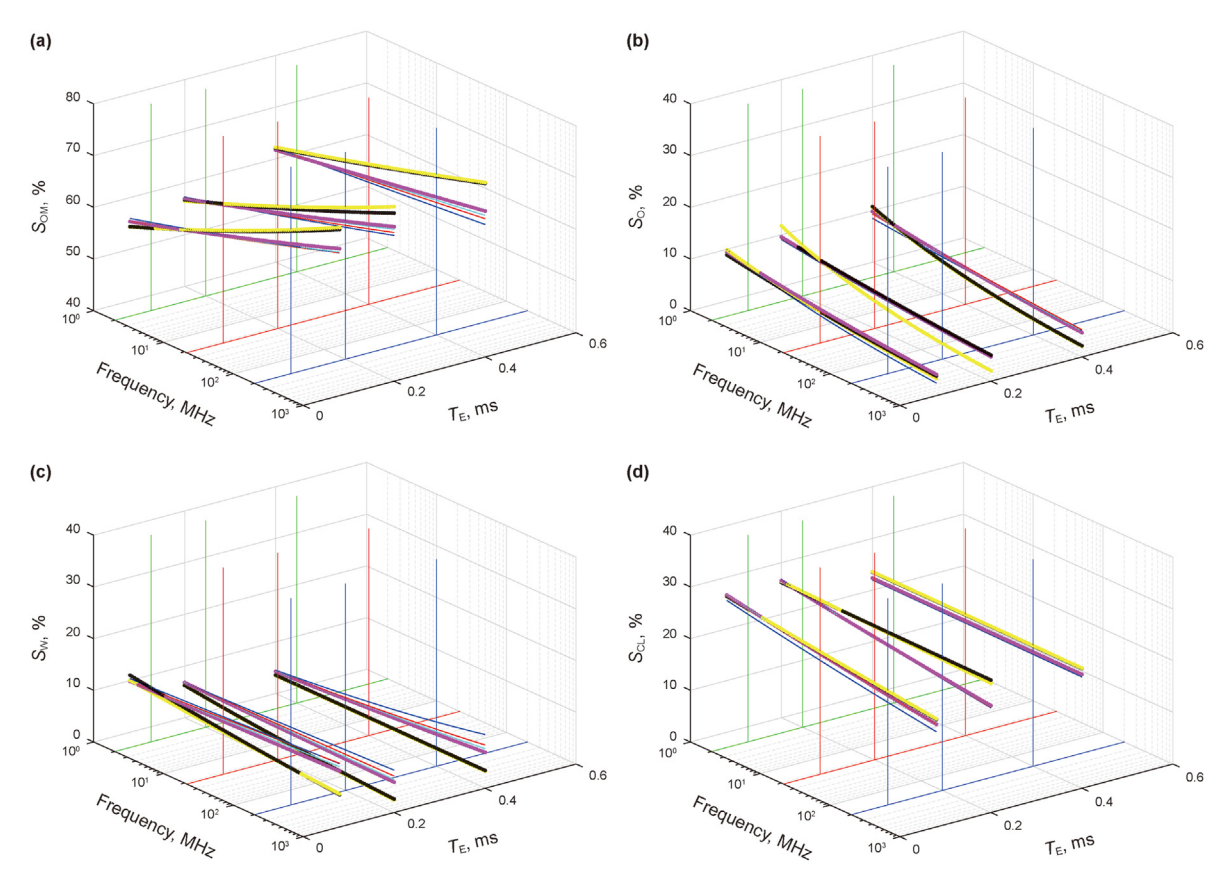


**Fig. 13.** Changes in OM saturation ( $S_{OM}$ ),  $S_O$ ,  $S_W$ , and  $S_{CL}$  with magnetic field frequency with varying pyrite contents. The blue solid line, red solid line, cyan dotted line, magnetic dash-dotted line, black dotted-line, and yellow dotted-line represent the changes in the saturation of each component with varying pyrite contents (0.55%, 1.77%, 2.68%, 3.94%, 5.3%, and 6.9%). (a), (b), (c) and (d) represent OM, oil, water, and clay-bound water, respectively. The blue, red, and green dashed lines are the boundary lines for 2, 21.36, and 200 MHz.

lead to accelerated echo decay, and the peaks of the  $T_1$ - $T_2$  spectra of oil and water would shift toward the upper left corner, due to which the determined  $S_{\rm O}$  and  $S_{\rm W}$  would be lower. As pyrite content increases and other parameters are unchangeable, the peaks of the  $T_1$ - $T_2$  spectra of oil and water would shift toward the upper left corner more obviously, and  $S_0$  and  $S_W$  would therefore decrease more rapidly. As shown in Fig. 13(d), S<sub>CL</sub> decreases slightly as magnetic field frequency increases and other parameters are unchangeable. Because when magnetic field frequency increases, the clay-bound water content remains unchanged, but the contents of OM, oil, and water would change. When the changes in OM content are greater than that in oil and water,  $S_{CL}$  would decrease. When the changes in OM content are close to that from oil and water,  $S_{CL}$ would be a fixed value. Therefore, for formations with high pyrite content, the changes in oil and IP water contents are close to the changes in OM contents, and the clay-bound water contents are close to a fixed value. When pyrite content is 5.3%, T<sub>E</sub> is 0.4 ms, and magnetic field frequency are 2, 21.36, and 200 MHz, respectively, the OM saturation are 63.1%, 66.9%, and 70.7%, which are 112.8%, 120.0%, and 126.4% of the OM saturation from the original shale cores. The S<sub>0</sub> are 8.18%, 6.11%, and 4.64%, which are 112.2%, 86.7%, and 67.9% of the  $S_0$  from the original shale cores. The  $S_W$  are 3.56%, 3.52%, and 3.48%, which are 34.1%, 41.0%, and 48.7% of the  $S_{\rm W}$  from the original shale cores. The  $S_{\rm CL}$  are 25.7%, 23.7%, and 22.0%, which are 91.3%, 98.4%, and 105.8% of the  $S_{WC}$  from the original shale

# 5.2. Petrophysical parameters frequency conversion for different clay contents

The changes in OM saturation,  $S_0$ ,  $S_W$ , and  $S_{CL}$  with magnetic field frequency under conditions of varying  $T_{\rm E}$  and clay contents were identified on the basis of the saturation results (Fig. 14(a)–(d). As shown in Fig. 14(a), OM saturation increases as magnetic field frequency increases and other parameters are unchangeable. As  $T_{\rm E}$ increases and other parameters are unchangeable, OM saturation decreases with low clay content and increases with high clay content (Fig. 14(a)). These results are not interpreted because they have been interpreted in previous section. As shown in Fig. 14(b) and (c),  $S_0$  and  $S_W$  decrease as magnetic field frequency increases and other parameters are unchangeable. When magnetic field frequency increases, the significantly enhanced diffusion relaxation of pore fluids would lead to accelerated echo decay, and the peaks of the  $T_1$ - $T_2$  spectra of oil and water would shift toward the upper left corner, due to which the determined *S*<sub>O</sub> and *S*<sub>W</sub> would be lower. As clay content increases and other parameters are unchangeable, the peaks of the  $T_1$ - $T_2$  spectra of Oil and IP water would shift toward the upper left corner more obviously, and S<sub>O</sub> and S<sub>W</sub> would therefore decrease more rapidly. As shown in Fig. 14(d), S<sub>CL</sub> decreases slightly as magnetic field frequency increases and other parameters are unchangeable. These results are not interpreted because they have been interpreted in previous section. When clay content is 10.49%, T<sub>E</sub> is 0.4 ms, and magnetic field frequency is 2,

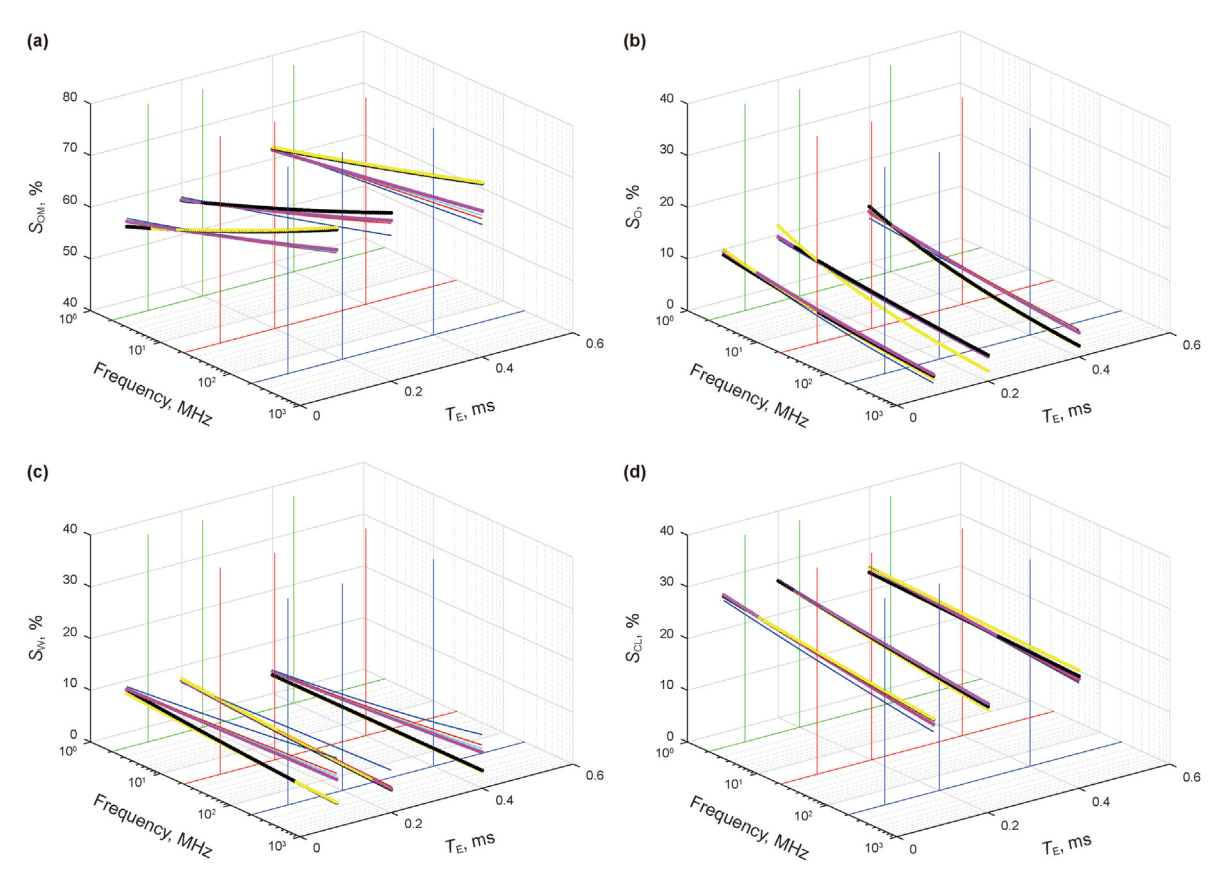


**Fig. 14.** Changes in  $S_{\rm OM}$ ,  $S_{\rm O}$ ,  $S_{\rm W}$ , and  $S_{\rm CL}$  with magnetic field frequency with varying clay contents. The blue solid, red solid, cyan dotted, magenta dash-dotted, black dotted, and yellow lines are the saturation variations from each component with varying pyrite contents (0%, 1.03%, 3.39%, 5.12%, 10.49%, and 20.14%). **(a)**, **(b)**, **(c)** and **(d)** represent OM, oil, water, and clay-bound water, respectively. The blue, red and green dashed lines are the boundary lines for 2, 21.36, and 200 MHz.

21.36, and 200 MHz, respectively, the OM saturation are 63.1%, 66.9%, and 70.7%, which are 112.8%, 108.6%, and 104.7% of OM saturation from the original shale cores. The  $S_{\rm O}$  are 9.17%, 5.29%, and 3.15%, which are 198.0%, 76.5%, and 60.4% of the  $S_{\rm O}$  from the original shale cores. The  $S_{\rm W}$  are 3.57%, 3.57%, and 3.56%, which are 46.1%, 55.9%, and 67.0% of the  $S_{\rm W}$  from the original shale cores. The  $S_{\rm CL}$  are 24.2%, 23.6%, and 23.0%, which are 94.3%, 99.5%, and 104.8% of the  $S_{\rm CL}$  from the original shale cores. It is to be noted that  $S_{\rm CL}$  changes with frequency, but it is not a fixed value, indicating that the effect of clay content on  $S_{\rm CL}$  is smaller than that of pyrite content. However, these effects are neglected for formations with high clay content.

# 5.3. Petrophysical parameters frequency conversion for different clay mineral types

The changes in OM saturation,  $S_{\rm O}$ ,  $S_{\rm W}$ , and  $S_{\rm CL}$  with frequency under conditions of varying  $T_{\rm E}$  and clay mineral type were identified on the basis of the saturation results (Fig. 15(a)—(d)). As shown in Fig. 15(a), OM saturation increases as magnetic field frequency increases and other parameters are unchangeable. As  $T_{\rm E}$  increases and other parameters are unchangeable, OM saturation decreases for clay minerals with low MS and increases for clay minerals with high MS (Fig. 15(a)). These results are not interpreted because they have been interpreted in previous section. As shown in Fig. 15(b) and (c),  $S_{\rm O}$  and  $S_{\rm W}$  decrease as magnetic field frequency increases and other parameters are unchangeable. When magnetic field frequency increases, the significantly enhanced diffusion relaxation of pore fluids would lead to accelerated echo decay, and the peaks

of the  $T_1$ - $T_2$  spectra of oil and water would shift toward the upper left corner, due to which the determined  $S_0$  and  $S_W$  would be lower. As the MS of clay minerals increases and other parameters are unchangeable, the peaks of the  $T_1$ - $T_2$  spectra of oil and water would shift toward the upper left corner more obviously, and  $S_0$  and  $S_W$  would therefore decrease more rapidly. As shown in Fig. 15(d),  $S_{CL}$  decreases slightly as magnetic field frequency increases while other parameters are unchangeable. These results are not interpreted because they have been interpreted in previous section. It should be noted that  $S_{CL}$  changes with frequency, but it is not close to a fixed value, indicating that the effect of clay mineral type on  $S_{CL}$  is smaller than that of pyrite content.

### 6. Discussion

In this work, according to the hypothesis that water only exists in the IP and oil only exists in the OP, we developed the  $T_1$ - $T_2$  numerical simulation methods in shale oil reservoirs with complex minerals, and the accuracy of numerical simulation was verified from NMR  $T_1$ - $T_2$  experiments from the parallel samples. The samples selected for the experiments showed heterogeneity. To minimize this variability, the parallel samples that closely matched the core used for the FIB-SEM experiment were selected. Meanwhile, the OM content, oil, and the water in the digital shale core from the FIB-SEM experiment were determined to be 22.36%, 0.55%, and 1.39% respectively. Due to the significant difference between the OM content and pore fluids, the simulation results showed strong signal intensity for OM, while the signal intensities of water and oil were comparatively weak. In actual shale formations, where the

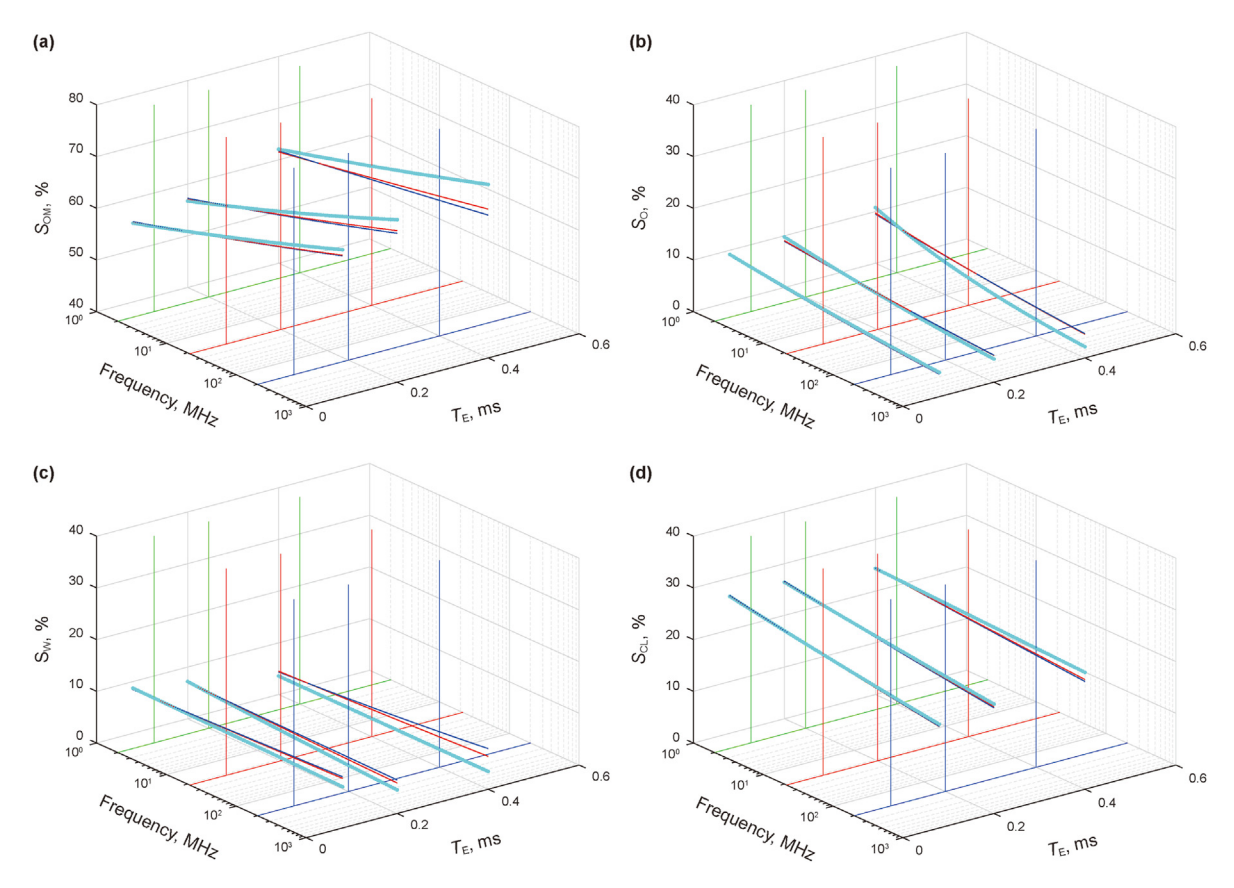


**Fig. 15.** Changes in  $S_{\rm OM}$ ,  $S_{\rm O}$ ,  $S_{\rm W}$ , and  $S_{\rm CL}$  with magnetic field frequency with varying clay mineral types. The dark blue solid, red dash-dotted, and cyan dotted lines represent the changes in the saturation of each component with varying clay mineral types. **(a)**, **(b)**, **(c)**, and **(d)** represent OM, oil, water, and clay-bound water, respectively. The blue, red, and green dashed lines are the boundary lines for 2, 21.36, and 200 MHz.

OM content is typically lower, the signal intensity of OM in the  $T_1$ - $T_2$  spectra remained low, particularly when  $T_{\rm E}$  is set to 0.4 ms or 0.2 ms. Actually, the occurrence state of fluids is also a key factor influencing the NMR responses of shale oil. Nevertheless, despite these challenges, this study still provides new insights into the 2-D  $T_1$ - $T_2$  responses in shale oil reservoirs across different frequencies. In the future, we will continue to explore the effects from occurrence state of fluids.

#### 7. Conclusions

In shale oil reservoirs,  $T_1$ - $T_2$  spectra are of great significance in characterizing the petrophysical properties. However, factors such as the highly non-uniform distributions of minerals and OM in shale affect NMR-based petrophysical properties characterization. Numerical simulations can effectively quantify these effects on the petrophysical properties. In addition, differences in frequency and acquisition parameters between laboratory NMR instruments and NMR logging also affect the NMR-based the petrophysical properties characterization.

In this study, for the first time, the NMR  $T_1$ – $T_2$  relaxation theory was developed on the basis of modified Korb's theory. The transverse and longitudinal relaxivities of pore fluids were determined from numerical simulations and experimental analysis (extraction, GC, multi-frequency NMR, and NMR 2-D  $T_1$ - $T_2$  experiments) conducted on digital shale cores. Based on digital core technology, the IRW algorithm was developed and used for the first time to simulate the effects of the HI of OM,  $T_E$ , pyrite content, clay mineral type, and clay content on  $T_1$ - $T_2$  spectra at different magnetic field

frequencies. Frequency conversion cross-plots for various petrophysical properties were established for the first time. The conclusions are as follows:

- (1) The modified Korb's theory describes the frequency dependences for  $T_{1B,K}$ ,  $T_{2B,K}$ ,  $\rho_{1S,O}$ ,  $\rho_{1S,W}$ ,  $\rho_{2S,O}$ ,  $\rho_{2S,W}$ , and the internal magnetic field gradient. This provides new ideas for the quantitative evaluation of the pore fluids in shale oil reservoirs, petrophysical characterization of shale oil, and frequency conversion for petrophysical parameters such as fluid saturation on the basis of  $T_1$ - $T_2$  spectra obtained from laboratory NMR instruments and field NMR logging.
- (2) The results of the  $T_1$ - $T_2$  numerical simulations performed with the developed Korb's theory show the HI of OM affects qualitative analysis of the pore fluids, and the  $T_{\rm E}$  should be minimized to reduce the impact of the diffusion relaxation. Factors such as magnetic field frequency, pyrite content, clay mineral type, and clay content affect the  $T_1$ - $T_2$  responses. The pyrite content has the greatest impact on the  $T_1$ - $T_2$  responses. When the pyrite content is 5.3%, the  $T_{\rm E}$  is 0.4 ms, and the magnetic field frequency are 2, 21.36, and 200 MHz, the OM saturation values are 63.1%, 66.9%, and 70.7%, which are 112.8%, 120.0%, and 126.4% of the OM saturation values from the original shale cores, respectively. Similarly, the oil saturation values are 8.18%, 6.11%, and 4.64%, respectively, which correspond to 112.2%, 86.7%, and 67.9% of the oil saturation values from the original shale cores. In addition, the IP water saturation values are 3.56%, 3.52%, and 3.48%, respectively, which correspond to 34.1%, 41.0%, and 48.7% of the IP  $S_{W}$

from the original shale cores. The  $S_{\rm CL}$  are 25.7%, 23.7%, and 22.0%, respectively, representing 91.3%, 98.4%, and 105.8% of the  $S_{\rm CL}$  from the original shale cores. Furthermore, when the magnetic susceptibility and content of clay increase, OM saturation increases,  $S_{\rm O}$ ,  $S_{\rm W}$ , and  $S_{\rm CL}$  decrease. In summary, compared with clay content and clay mineral type, pyrite content has a greater impact on the  $T_1$ - $T_2$  responses.

(3) Petrophysical parameters such as OM saturation, the  $S_{\rm O}$ ,  $S_{\rm W}$ , and  $S_{\rm CL}$  are affected by the pyrite contents and clay minerals under conditions of varying NMR frequencies and  $T_{\rm E}$ . Based on the results of numerical simulations, the frequency-conversion of petrophysical parameters including fluids saturation can be achieved to accurately determine  $S_{\rm O}$ ,  $S_{\rm W}$ , and  $S_{\rm CL}$ .

This study could be of great significance for quantitatively evaluating the saturation for fluids, the petrophysical characterization, and frequency conversion for petrophysical parameters using both laboratory NMR instruments and field NMR logging in shale oil reservoirs. It could play an important role in enhancing the recovery rate of fluids. In this paper, the NMR  $T_1$ - $T_2$  relaxation theory proposed could serve as a foundation for understanding how NMR responses may be altered during the displacement of other fluids by  $CO_2$  injection into shale reservoirs. Therefore, NMR technology could be used to monitor the sequestration of  $CO_2$ .

#### **CRediT authorship contribution statement**

**Ji-Long Liu:** Writing — original draft, Software, Resources, Methodology, Investigation, Formal analysis, Data curation. **Ran-Hong Xie:** Writing — review & editing, Validation, Supervision, Project administration, Funding acquisition. **Jiang-Feng Guo:** Writing — review & editing, Visualization, Validation. **Guo-Wen Jin:** Visualization, Validation, Supervision, Software.

## **Declaration of competing interest**

The authors declare that they have no known competing financial interests or personal relationships that could have appeared to influence the work reported in this paper.

#### Acknowledgements

This work was funded by the National Natural Science Foundation of China (42174131),

#### List of abbreviation

HI Hydrogen index OM Organic matter IP Inorganic pore OP Organic pore

IR-CPMG Inversion recovery-Carr-Purcell-Meiboom-Gill FIB-SEM Focused ion beam scanning electron microscope GC Extraction and gas chromatography experiments

IRW Improved random walk

HI Hydrogen index

T<sub>E</sub> Echo spacing

S<sub>O</sub> Saturation of oil

S<sub>W</sub> Saturation of water

S<sub>CL</sub> Saturation of clay bound water S<sub>OM</sub> Saturation of organic matter

#### References

- Benamsili, L., Korb, J.P., Hamon, G., et al., 2014. Multi-dimensional nuclear magnetic resonance characterizations of dynamics and saturations of brine/crude oil/mud filtrate mixtures confined in rocks: the role of asphaltene. Energy Fuels 28 (3), 1629–1640. https://doi.org/10.1021/ef401871h.
- Bloembergen, N., Purcell, E.M., Pound, R.V., 1948. Relaxation effects in nuclear magnetic resonance absorption. Phys. Rev. 73 (7), 679. https://doi.org/10.1103/ PhysRev.73.679.
- Butler, J.P., Reeds, J.A., Dawson, S.V., 1981. Estimating solutions of first kind integral equations with nonnegative constraints and optimal smoothing. SIAM J. Numer. Anal. 18, 381–397. https://doi.org/10.1137/0718025.
- Chi, L., Heidari, Z., Garcia, A.P., 2015. Investigation of wettability and fluid distribution in organic-rich mudrocks using NMR two-phase simulation. In: SPE Annual Technical Conference and Exhibition. https://doi.org/10.2118/175077-MS
- Dou, F., Wang, J.G., 2022. A numerical investigation for the impacts of shale matrix heterogeneity on hydraulic fracturing with a two-dimensional particle assemblage simulation model. J. Nat. Gas Sci. Eng. 104, 104678. https://doi.org/10.1016/j.jngse.2022.104678.
- Esen, M., Yuksel, T., 2013. Experimental evaluation of using various renewable energy sources for heating a greenhouse. Energy Buildings 65, 340–351. https://doi.org/10.1016/j.enbuild.2013.06.018.
- Fleury, M., Kohler, E., Norrant, F., et al., 2013. Characterization and quantification of water in smectites with low-field NMR. J. Phys. Chem. C 117 (9), 4551–4560. https://doi.org/10.1021/jp311006q.
- Fleury, M., Romero-Sarmiento, M., 2016. Characterization of shales using  $T_1$ – $T_2$  NMR maps. J. Petrol. Sci. Eng. 137, 55–62. https://doi.org/10.1016/j.petrol.2015.11.006.
- Guo, J., Xie, R., 2019. Numerical investigations of NMR  $T_1$ — $T_2$  map in two-phase fluid-bearing tight sandstone. Appl. Magn. Reson. 50, 479—495. https://doi.org/10.1007/s00723-018-1098-7.
- Guo, J., Xie, R., Xiao, L., 2020. Pore-fluid characterizations and microscopic mechanisms of sedimentary rocks with three-dimensional NMR: tight sandstone as an example. J. Nat. Gas Sci. Eng. 80, 103392. https://doi.org/10.1016/j.jngse.2020.103392.
- Gu, M., Xie, R., Jin, G., et al., 2021. Quantitative evaluation for fluid components on 2D NMR spectrum using Blind Source Separation. J. Magn. Reson. 332, 107079. https://doi.org/10.1016/j.jmr.2021.107079.
- Hu, T., Pang, X., Jiang, S., et al., 2018. Oil content evaluation of lacustrine organic-rich shale with strong heterogeneity: a case study of the Middle Permian Lucaogou Formation in Jimusaer Sag, Junggar Basin, NW China. Fuel 221, 196–205. https://doi.org/10.1016/j.fuel.2018.02.082.
- Jiang, H., Daigle, H., Zhang, B., et al., 2018. Characterization of thermal evolution of pores and fluids in shales using NMR 2D measurement. In: The SPE/AAPG/SEG Unconventional Resources Technology Conference. https://doi.org/10.15530/ LINTEC.2018-2001623
- Jiang, H., Daigle, H., Tian, X., et al., 2019. A comparison of clustering algorithms applied to fluid characterization using NMR  $T_1$ - $T_2$  maps of shale. COMPUT GEOSCI-UK 126, 52–61. https://doi.org/10.1016/j.cageo.2019.01.021.
- Jiang, H., Liu, S., Wang, J., et al., 2023. Study on evolution mechanism of the pyrolysis of chang 7 oil shale from Ordos basin in China. Energy 272, 127097. https:// doi.org/10.1016/j.energy.2023.127097.
- Kausik, R., Minh, C.C., Zielinski, L., et al., 2011. Characterization of gas dynamics in kerogen nanopores by NMR. In: SPE Annual Technical Conference and Exhibition. Denver, Colorado, USA, October, 2011. https://doi.org/10.2118/147198-MS.
- Kausik, R., Fellah, K., Feng, L., et al., 2017. High-and low-field NMR relaxometry and diffusometry of the bakken petroleum system. Petrophysics 58 (4), 341–351. https://onepetro.org/petrophysics/article/58/04/341/171402.
- Kausik, R., Fellah, K., Feng, L., et al., 2018. Temperature dependence of 2D NMR T<sub>1</sub>-T<sub>2</sub> maps of shale. SPWLA 59th Annual Logging Symposium. https://onepetro.org/SPWLAALS/proceedings/SPWLA18/5-SPWLA18/D053S011R003/28855.
- Korb, J.P., Malier, L., Cros, F., et al., 1996. Surface dynamics of liquids in nanopores. Phys. Rev. Lett. 77 (11), 2312. https://doi.org/10.1103/PhysRevLett.77.2312.
- Korb, J.P., Whaley-Hodges, M., Bryant, R.G., 1997. Translational diffusion of liquids at surfaces of microporous materials: theoretical analysis of field-cycling magnetic relaxation measurements. Phys. Rev. 56 (2), 1934. https://doi.org/10.1103/ PhysRevE.56.1934.
- Korb, J.P., Hodges, M.W., Gobron, T., et al., 1999. Anomalous surface diffusion of water compared to aprotic liquids in nanopores. Phys. Rev. 60 (3), 3097. https:// doi.org/10.1103/PhysRevE.60.3097.
- Korb, J.P., Nicot, B., Louis-Joseph, A., et al., 2014. Dynamics and wettability of oil and water in oil shales. J. Phys. Chem. C 118 (40), 23212–23218. https://doi.org/ 10.1021/ip508659e.
- Korb, J.P., Vorapalawut, N., Nicot, B., et al., 2015. Relation and correlation between NMR relaxation times, diffusion coefficients, and viscosity of heavy crude oils. J. Phys. Chem. C 119 (43), 24439–24446. https://doi.org/10.1021/ acs.ipcc.5b07510.
- Korb, J.P., 2018. Multiscale nuclear magnetic relaxation dispersion of complex liquids in bulk and confinement. Prog. Nucl. Magn. Reson. Spectrosc. 104, 12–55. https://doi.org/10.1016/j.pnmrs.2017.11.001.
- Li, J., Jiang, C., Wang, M., et al., 2020. Adsorbed and free hydrocarbons in unconventional shale reservoir: a new insight from NMR  $T_1$ – $T_2$  maps. Mar. Petrol. Geol. 116, 104311. https://doi.org/10.1016/j.marpetgeo.2020.104311.

- Lipari, G., Szabo, A., 1982. Model-free approach to the interpretation of nuclear magnetic resonance relaxation in macromolecules. 1. Theory and range of validity. J. Am. Chem. Soc. 104 (17), 4546–4559. https://doi.org/10.1021/ ia00381a009.
- Liu, J., Yang, Y., Sun, S., et al., 2022. Flow behaviors of shale oil in kerogen slit by molecular dynamics simulation. Chem. Eng. J. 434, 134682. https://doi.org/ 10.1016/j.cej.2022.134682.
- Liu, J., Xie, R., Guo, J., et al., 2023. Multicomponent digital core construction and three-dimensional micro-pore structure characterization of shale. Phys. Fluids 35, 082003. https://doi.org/10.1063/5.0155425.
- Liu, J., Xie, R., Guo, J., 2024a. Numerical investigation of  $T_2^*$ -based and  $T_2$ -based petrophysical parameters frequency-dependent in shale oil. Energy 313, 133788. https://doi.org/10.1016/j.energy.2024.133788.
- Liu, J., Xie, R., Guo, J., 2024b. Pore-scale T<sub>2</sub>-based numerical investigation on dynamics and wettability in mixed-wet shale oil reservoirs. Phys. Fluids 36, 122025. https://doi.org/10.1063/5.0247232.
- Liu, J., Xie, R., Guo, J., et al., 2024c. Study of nuclear magnetic resonance response mechanism in shale oil and correction of petrophysical parameters. Fuel 358, 130162. https://doi.org/10.1016/j.fuel.2023.130162.
- Ma, Y., Wang, H., Wang, W., et al., 2020. The application of Nuclear Magnetic Resonance T<sub>1</sub>-T<sub>2</sub> maps in the research of sedimentary organic matter: a case study of early mature shale with type I kerogen. J. Petrol. Sci. Eng. 194, 107447. https://doi.org/10.1016/j.petrol.2020.107447.
- Nie, B., 2023. Study on thermal decomposition of oil shale: two-phase fluid simulation in wellbore. Energy 272, 127124. https://doi.org/10.1016/i.energy.2023.127124.
- Osiptsov, A.A., 2017. Fluid mechanics of hydraulic fracturing: a review. J. Petrol. Sci. Eng. 156, 513–535. https://doi.org/10.1016/j.petrol.2017.05.019.
- Singer, P.M., Chen, Z., Alemany, L.B., et al., 2018. Interpretation of NMR relaxation in bitumen and organic shale using polymer—heptane mixes. Energy Fuels 32 (2), 1534—1549. https://doi.org/10.1021/acs.energyfuels.7b03603.
- Singer, P.M., Valiya Parambathu, A., Wang, X., et al., 2020. Elucidating the <sup>1</sup>H NMR relaxation mechanism in polydisperse polymers and bitumen using measurements, MD simulations, and models. J. Phys. Chem. B 124 (20), 4222–4233. https://doi.org/10.1021/acs.jpcb.0c01941.
- Silletta, E.V., Vila, G.S., Domené, E.A., et al., 2022. Organic matter detection in shale reservoirs using a novel pulse sequence for  $T_1$ - $T_2$  relaxation maps at 2 MHz. Fuel 312, 122863. https://doi.org/10.1016/j.fuel.2021.122863.
- Sun, F., Yao, Y., Chen, M., et al., 2017. Performance analysis of superheated steam injection for heavy oil recovery and modeling of wellbore heat efficiency. Energy 125, 795–804. https://doi.org/10.1016/j.energy.2017.02.114.
- Sun, F., Yao, Y., Li, G., et al., 2018a. Geothermal energy extraction in CO<sub>2</sub> rich basin using abandoned horizontal wells. Energy 158, 760–773. https://doi.org/10.1016/j.energy.2018.06.084.
- Sun, F., Yao, Y., Li, X., 2018b. The heat and mass transfer characteristics of superheated steam coupled with non-condensing gases in horizontal wells with multi-point injection technique. Energy 143, 995–1005.
- Tandon, S., Heidari, Z., Matenoglou, G., 2017. Pore-scale numerical modeling of nuclear magnetic resonance response in rocks with complex pore structure using finite volume method. SPWLA 58th Annual Logging Symposium. In: https://onepetro.org/SPWLAALS/proceedings/SPWLA17/5-SPWLA17/ D053S013R010/28606.

- Tandon, S., Heidari, Z., 2019. Quantifying the mechanisms contributing to nuclear-magnetic-resonance surface relaxation of protons in kerogen pores of organic-rich mudrocks. SPE J. 24 (6), 2438–2457. https://doi.org/10.2118/197063-PA.
- Van Erdeweghe, S., Van Bael, J., Laenen, B., et al., 2018. Optimal combined heat-and-power plant for a low-temperature geothermal source. Energy 150, 396–409. https://doi.org/10.1016/j.energy.2018.01.136.
- Wang, L., Liu, B., Bai, L.H., et al., 2023a. Maceral evolution of lacustrine shale and its effects on the development of organic pores during low mature to high mature stage: a case study from the Qingshankou Formation in northern Songliao Basin, northeast China. Pet. Sci. 20 (5), 2709–2725. https://doi.org/10.1016/ i.petsci.2023.08.025.
- Wang, Y., Chang, X.C., Liu, Z.Q., et al., 2023b. Occurrence state and oil content evaluation of Permian Fengcheng Formation in the Hashan area as constrained by NMR and multistage Rock-Eval. Pet. Sci. 20 (3), 1363—1378. https://doi.org/10.1016/j.petsci.2022.11.019.
- Washburn, K.E., 2014. Relaxation mechanisms and shales. CONCEPT MAGN RESON. A 43 (3), 57–78. https://doi.org/10.1002/cmr.a.21302.
- Washburn, K.E., Birdwell, J.E., 2013. Updated methodology for nuclear magnetic resonance characterization of shales. J. Magn. Reson. 233, 17–28. https:// doi.org/10.1016/j.jmr.2013.04.014.
- Washburn, K.E., Mu, Y., Toelke, J., 2015. Simulating the nuclear magnetic resonance response in organic rich shales. In: Unconventional Resources Technology Conference. https://doi.org/10.15530/urtec-2015-2154947.
- Xu, C., Xie, R., Guo, J., et al., 2023. Comprehensive characterization of petrophysical properties in shale by solvent extraction experiments and 2D NMR. Fuel 335, 127070. https://doi.org/10.1016/j.fuel.2022.127070.
- Xu, S., Sun, Y., Guo, W., et al., 2023. Regulating the oxidative assisted pyrolysis of Huadian oil shale by preheating temperature and oxygen flow rate. Energy 262, 125602. https://doi.org/10.1016/j.energy.2022.125602.
- Yang, Z., Hirasaki, G.J., 2008. NMR measurement of bitumen at different temperatures. J. Magn. Reson. 192 (2), 280–293. https://doi.org/10.1016/j.jmr.2008.03.007.
- Yang, Z., Hirasaki, G.J., Appel, M., et al., 2012. Viscosity evaluation for NMR well logging of live heavy oils. Petrophysics 53 (1), 22–37. https://onepetro.org/petrophysics/article-abstract/53/01/22/171242.
- Zamiri, M.S., Marica, F., Romero-Zerón, L., et al., 2022. Monitoring shale water uptake using 2D magnetic resonance relaxation correlation and sprite MRI. Chem. Eng. J. 428, 131042. https://doi.org/10.1016/j.cej.2021.131042.
- Zhang, B., Daigle, H., 2017. Nuclear magnetic resonance surface relaxation mechanisms of kerogen. Geophysics 82 (6), JM15–JM22. https://doi.org/10.1190/geo2016-0350.1.
- Zhang, P., Lu, S., Li, J., et al., 2020. 1D and 2D Nuclear magnetic resonance (NMR) relaxation behaviors of protons in clay, kerogen and oil-bearing shale rocks. Mar. Petrol. Geol. 114, 104210. https://doi.org/10.1016/j.marpetgeo.2019.104210.
- Zhan, H., Wang, Y., Chen, M., et al., 2020. An optical mechanism for detecting the whole pyrolysis process of oil shale. Energy 190, 116343. https://doi.org/10.1016/j.energy.2019.116343.
- Zhu, C., Guo, W., Li, Y., et al., 2021. Effect of occurrence states of fluid and pore structures on shale oil movability. Fuel 288, 119847. https://doi.org/10.1016/ i.fuel.2020.119847.